

PAPER • OPEN ACCESS

# Investigation of helium exhaust dynamics at the ASDEX Upgrade tokamak with full-tungsten wall











To cite this article: A. Zito *et al* 2023 *Nucl. Fusion* **63** 096027

View the [article online](#) for updates and enhancements.

You may also like

- [Enhancement of helium exhaust by resonant magnetic perturbation fields at LHD and TEXTOR](#)  
O. Schmitz, K. Ida, M. Kobayashi *et al.*
- [Overview of L- to H-mode transition experiments at ASDEX Upgrade](#)  
U Plank, R M McDermott, G Birkenmeier *et al.*
- [Development and application of a predictive model for advanced tokamak scenario design](#)  
Raphael Schramm, Alexander Bock, Emiliano Fable *et al.*

# Investigation of helium exhaust dynamics at the ASDEX Upgrade tokamak with full-tungsten wall

A. Zito<sup>1,2,\*</sup> , M. Wischmeier<sup>1</sup>, A. Kappatou<sup>1</sup> , A. Kallenbach<sup>1</sup> , F. Sciortino<sup>1</sup> , V. Rohde<sup>1</sup>, K. Schmid<sup>1</sup>, E.T. Hinson<sup>3</sup> , O. Schmitz<sup>3</sup> , M. Cavedon<sup>4</sup> , R.M. McDermott<sup>1</sup> , R. Dux<sup>1</sup>, M. Griener<sup>1</sup> , U. Stroth<sup>1,2</sup>  and the ASDEX Upgrade Team<sup>a</sup>

<sup>1</sup> Max Planck Institute for Plasma Physics, Boltzmannstr. 2, 85748 Garching, Germany

<sup>2</sup> Physik-Department E28, Technische Universität München, Garching, Germany

<sup>3</sup> University of Wisconsin-Madison, Madison, WI 53706, United States of America

<sup>4</sup> Dipartimento di Fisica G. Occhialini, Università di Milano-Bicocca, Milano, Italy

E-mail: [antonello.zito@ipp.mpg.de](mailto:antonello.zito@ipp.mpg.de)

Received 4 April 2023, revised 26 June 2023

Accepted for publication 28 June 2023

Published 11 August 2023



CrossMark

## Abstract

An efficient removal of He ash by active pumping in future fusion devices is necessary to avoid fuel dilution and not degrade the core confinement properties. Therefore, a deep understanding of the underlying physics mechanisms is mandatory. Helium exhaust has been experimentally investigated at the ASDEX Upgrade tokamak. This is an ideal test environment, thanks to the ITER-like divertor geometry, an extensive diagnostics coverage and the presence of plasma-facing components made of tungsten. The exhaust efficiency, characterized by the He compression in the divertor, was found to improve with increasing divertor neutral pressure but to degrade with detachment. A multi-reservoir particle balance model was developed to interpret the observed exhaust dynamics, accounting for plasma transport and wall retention. The limited performance of the pumping system and the efficient helium retention capability of the tungsten wall were identified to have the strongest impact on the exhaust dynamics.

Keywords: helium exhaust, helium compression, helium enrichment, divertor retention, pumping, wall storage, ASDEX Upgrade

(Some figures may appear in colour only in the online journal)

## 1. Introduction

Understanding helium exhaust is critical for the design of future fusion devices. The concentration of He ‘ash’ produced

in the core plasma by fusion reactions must be kept within tolerable values to avoid fuel dilution. A mathematical model for stationary burning suggests that the ratio between global residence time of He particles in the plasma  $\tau_{\text{He}}^*$  and energy confinement time  $\tau_E$  should be kept in the range 7–15 for a D–T plasma [1–4]. In the design of ITER, a maximum limit of ten is foreseen for such a ratio [5]. A degradation of the confinement performance has also been systematically seen in different currently operating devices with increasing He impurity content in hydrogenic plasmas [6–8].

A mechanism to flush He ash from the plasma arises from the recycling of He ions at the plasma-facing material surfaces and the subsequent pumping of these in the form of

<sup>a</sup> See Stroth *et al* 2022 (<https://doi.org/10.1088/1741-4326/ac207f>) for the ASDEX Upgrade Team.

\* Author to whom any correspondence should be addressed.



Original Content from this work may be used under the terms of the [Creative Commons Attribution 4.0 licence](https://creativecommons.org/licenses/by/4.0/). Any further distribution of this work must maintain attribution to the author(s) and the title of the work, journal citation and DOI.

neutral atoms. For this to occur, He particles must be (a) efficiently transported toward the plasma edge, (b) neutralized at the plasma-facing material surfaces, and (c) collected by an active pumping system before they are reionized. Whereas the first requirement is mostly linked with the physics of transport processes, the other two depend on the choice of geometry and materials for plasma-facing components (PFCs) and on the pump design, and therefore they allow more room for optimization.

From this point of view, exhaust is optimized when leakage of neutralized He atoms from the divertor volume toward the main chamber is minimized. This allows large He neutral pressures in the neutral gas in front of the pumping surfaces. A machine-independent parameter describing this is the compression, defined as

$$C_{\text{He}} \equiv \frac{n_{\text{He}^0}^{\text{div}}}{n_{\text{He}^{2+}}^{\text{plasma}}} \quad (1)$$

i.e. the ratio between He particle content in the exhaust gas and average He ion content in the confined plasma. A further parameter is the enrichment, defined as

$$\eta_{\text{He}} \equiv \frac{C_{\text{He}}}{C_{\text{D-T}}} \quad (2)$$

i.e. the ratio between He compression and main fuel (D–T) compression. While  $C_{\text{He}}$  is a figure of merit for the efficiency of helium exhaust alone,  $\eta_{\text{He}}$  instead relates it to the exhaust of the main fuel. High values of both  $C_{\text{He}}$  and  $\eta_{\text{He}}$  are desired to satisfy the requirement of efficient helium flushing from the plasma while simultaneously optimizing the throughput of the main fuel. This is important to ensure adequate particle control and to optimize the T fuel cycle [9]. According to the most recent ITER design studies,  $\eta_{\text{He}}$  must not be lower than 0.1–0.2 [5].

Measuring such quantities in He-seeded hydrogenic plasmas allows us to understand the helium exhaust mechanisms to optimize the operation of future devices. Experiments have been performed in several diverted tokamaks, including the JET [10–12], ASDEX Upgrade [13–15], JT-60U [16], and DIII-D [17, 18]. These studies have generally shown that helium exhaust is not constrained by core transport in ITER-relevant H-mode plasmas but is limited by edge phenomena, namely helium transport efficiency in the scrape-off layer (SOL) and external pumping. The exhaust is mostly enhanced, optimizing the divertor geometry, i.e. maximizing the amount of recycled He atoms which are directly scattered toward the pumps and minimizing their backflow toward the plasma. An increase in He compression and a decrease in He enrichment are also generally seen in higher recycling divertor regimes, at least before the detachment onset. These findings were supported by interpretative numerical modeling [19, 20] and taken into account in the design of the ITER divertor [21–24].

This work reports on revisited helium exhaust investigations carried out at the AUG tokamak. The divertor target geometry has been renewed since the previous investigation

[13–15], and the full-C wall has been replaced by a full-W wall. This allows for the investigation of helium recycling from a more fusion-relevant material [25]. Tungsten has also been proven to have a higher storage capability for He atoms w.r.t. carbon [26]. The consequent wall retention of helium is then expected to have a greater impact on the plasma behavior than the one observed in the full-C AUG.

We performed dedicated experiments featuring injection of helium through gas puff into otherwise steady-state D plasmas. We measured the global exhaust parameters (compression and enrichment), which allowed us to quantify divertor retention for helium.

We then focused on the interpretation of the exhaust dynamics by modeling the time evolution of the experimentally observed He concentrations. To characterize how wall retention affects the helium behavior in AUG plasmas, we developed a numerical model that self-consistently couples impurity transport in the plasma and long-term wall storage, taking into account the plasma–wall interactions in a realistic manner. This allowed us to disentangle the impact of wall retention and active pumping on the observed dynamic behavior of helium in the plasma.

In section 2, the experimental results are presented, including the employed experimental setup, the documentation of the performed discharges, and the measurements of He compression and enrichment. Section 3 provides a brief possible interpretation of the observed divertor helium retention. In section 4, the employed numerical model is described. In section 5, the modeling results are presented, and the consequent interpretation of the experimentally observed He exhaust dynamics is discussed. Section 6 gives a summary of the results and an outlook.

## 2. Experimental studies

The experiments presented in this work were all carried out at AUG [27]. All investigated discharges were lower single-null type-I ELMy H-modes with D fueling and with toroidal magnetic field  $B_t = -2.5$  T, edge safety factor  $q_{95} = 5.1$ – $5.3$ , and plasma current  $I_p = 0.8$  MA. Figure 1 shows a typical poloidal cross section of the employed edge-optimized equilibrium. The applied electron cyclotron resonance heating (ECRH) heating power was about 2 MW, while the applied neutral beam injection (NBI) heating power ranged from 7.5 to 10 MW.

In all discharges, we puffed He into an otherwise steady-state background D plasma. These experiments were aimed to measure the relative He concentration both in the plasma and in the exhaust gas in different divertor conditions, namely neutral pressures and detachment states. This allowed us to estimate the resulting compression and enrichment and to have a solid experimental foundation for modeling and interpreting the exhaust dynamics.

Although the focus was not on helium core transport, as this does not heavily impact the exhaust properties [13], we consistently observed He ion density profiles in the core

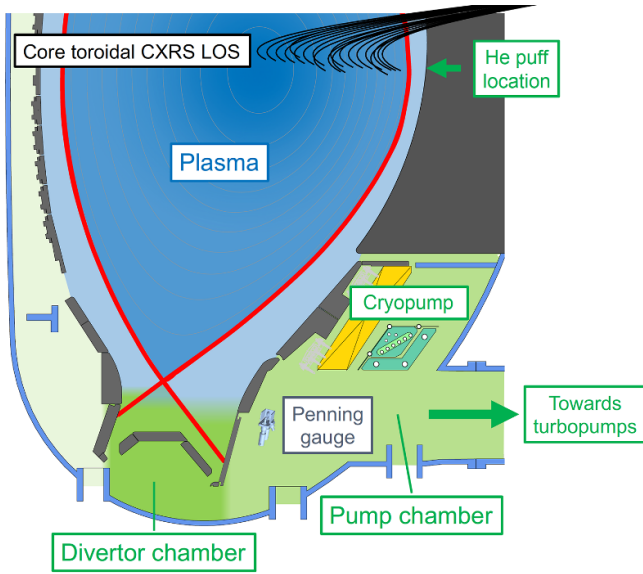


**Figure 1.** Poloidal view of the central-lower section of the AUG. Employed diagnostics, pumping systems, and region definitions as used in the text are highlighted. Regions dominated by the presence of ionized particles are filled in blue, while regions dominated by the presence of the neutral gas are filled in green. Such color code for ions/neutrals applies for all the figures present in the text. CXRS, charge exchange recombination spectroscopy; LOS, line of sight.

slightly less peaked than the electron density profiles. This is in agreement with past experimental findings, considering that external heating in our discharges always features a high NBI fraction [28].

### 2.1. AUG pumping systems

The main pumping effect at AUG is given by a toroidally symmetric cryopump [29], providing a pumping speed for deuterium of about  $120 \text{ m}^3 \text{ s}^{-1}$  [30]. This is not effective in pumping helium, as it does not condense on the cryopanel surface. Adsorption of helium may be triggered by employing argon to form a frosted cryotrapping surface [31], as already shown in other devices [12]. However, attempts at argon frost at the AUG cryopump have been so far unsuccessful, mostly leading to a strong argon contamination of the plasma. The only active helium removal effect is given by a turbomolecular pumping system, providing a pumping speed of about  $7 \text{ m}^3 \text{ s}^{-1}$  [30].

### 2.2. Relevant diagnostics

A charge exchange recombination spectroscopy (CXRS) system [32] provided spatially and temporally resolved He ion density profiles in the core plasma. We employed a recently developed framework for the routine evaluation of impurity densities [33], based on the ADAS effective charge exchange (CX) emission rates [34]. In the evaluation of the absolute He ion density, the plume effect [35] is taken into account [36].

The line of sight of the employed spectrometer, covering the full outer plasma midplane, is shown in black in figure 1.

In the following, we will often refer to an average core He ion density, used in the definition of a zero-dimensional He compression ratio (equation (1)). This is obtained by radially integrating the midplane profile along the normalized poloidal flux coordinate  $\rho$  as

$$\begin{aligned} \bar{n}_{\text{He}^{2+}}^{\text{plasma}} &\equiv \frac{\int_{\text{core}} n_{\text{He}^{2+}}(\mathbf{x}) d^3\mathbf{x}}{\int_{\text{core}} d^3\mathbf{x}} \approx \frac{\int_0^1 n_{\text{He}^{2+}}(\rho) 2\pi \rho 2\pi R_0 d\rho}{\int_0^1 2\pi \rho 2\pi R_0 d\rho} \\ &\approx 2 \int_0^1 \rho n_{\text{He}^{2+}}(\rho) d\rho. \end{aligned} \quad (3)$$

For the calculation of the neutral He content in the exhaust gas, we employed a newly developed type of *in situ* Penning gauge, similar to that described in [37]. Applying a voltage of a few kilovolts to the anode of the magnetic-field-aligned probe head of the gauge, an electrical discharge of the order of several milliamperes was sustained in the gauge chamber [38]. The resulting excitation of the neutral gas allowed us to spectroscopically observe the line intensities of the present gas species and to resolve the relative partial pressures. To this end, the  $D_\alpha$  Balmer line at 656.2 nm and the HeI line for the  $1s3d \rightarrow 1s2p$  singlet transition at 667.8 nm are observed.

In past exhaust studies, He partial pressure has been generally measured by gauges mounted at the outer peripheries of the devices [39]. Instead, the gauge mounted at AUG is located within the vessel volume, directly in front of the pumping surfaces (figure 1). This allows the response time of the measurement to be compatible with the characteristic impurity residence times in the plasma and in the divertor region. This is a fundamental ingredient for the detailed dynamic investigation, which is presented in the following sections.

We converted the measured He partial pressure in neutral He atom density, used in equation (1), employing the assumption of an ideal gas at room temperature. This is consistent with the usually observed neutral gas pressures at the AUG divertor (of the order of a few Pa at most) and supported by kinetic neutral gas modeling.

### 2.3. Helium exhaust and divertor neutral pressure

The first series of performed experiments was aimed to investigate the impact of divertor neutral pressure on helium exhaust. This is generally seen as the main figure of merit affecting impurity retention in the divertor at AUG [40, 41].

We performed three discharges with constant feedback-controlled divertor neutral gas pressure, at otherwise constant parameters, including equilibrium and heating. Figure 2 shows the main traces. The modulation scheme employed for the NBI beams was used to facilitate the estimation of the passive CXRS emission signals, in the evaluation of the absolute He ion density [28].

The different feedback-requested divertor pressure levels resulted in different D fueling levels. In all discharges, we

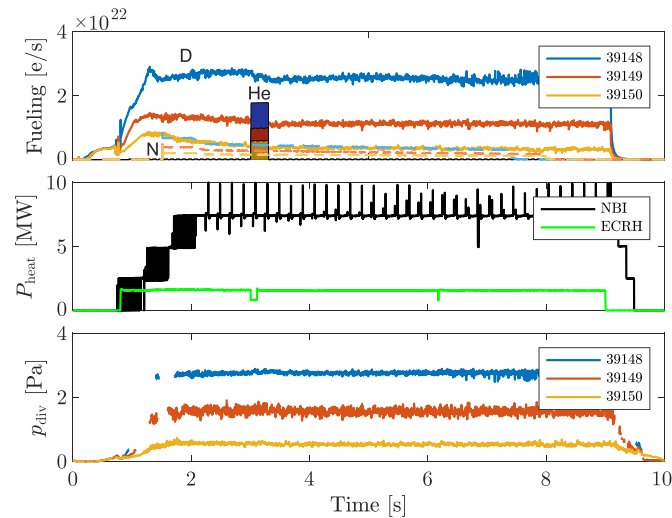


**Figure 2.** Some time traces from the performed divertor pressure scan. From top to bottom: fueling (D as solid lines, N as dashed lines, and He as filled areas, the last ones magnified four times w.r.t. the actual value), heating power (common for all the discharges), and divertor pressure.

applied a 300 ms long He puff, with injection performed from a midplane fueling valve. The He fueling rate was scaled with the expected D gas puff to achieve a similar peak He concentration in the core of roughly 10%–12%. We also employed moderate N seeding for diagnostic purposes ( $T_i$  and  $v_{rot}$  measurements).

The divertor pressure, measured by the ASDEX-type ionization gauges [42], refers to the *divertor chamber* located below the roof baffle and directly coupled with the recycling region from the divertor targets. This is connected to a different region, here called *pump chamber*, from which the pumping is actually performed (and where the employed *in situ* Penning gauge sits). See figure 1 for the definition of the two regions. The flow between the two chambers is conductance limited [41], resulting in measured pressure drops between the two chambers of about three to five for deuterium for the investigated pressure range and about two for helium. This difference is explained by the presence of the cryopump as an additional sink for deuterium, which instead is ineffective for helium.

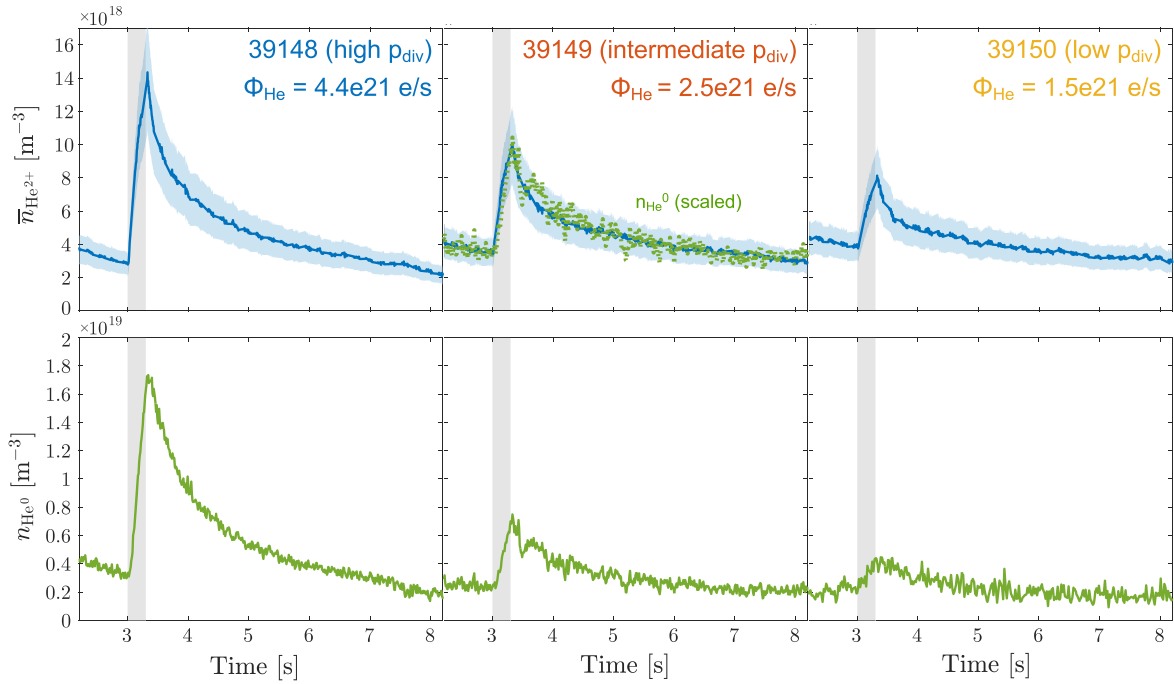
Figure 3 shows the measured average He ion density in the core plasma and the He neutral atom density in front of the pumping surface for the three performed discharges. At the beginning of the diagnosed part of the discharge, before the active injection phase, a relevant amount of He ions (with a relative concentration about 1%–2%) is already present in the plasma. Without external injection, the only remaining possible source is the release of He atoms implanted in the plasma-wetted surfaces of the W wall. After the active injection phase, active pumping makes the He ion content in the plasma fall down to its initial value only within the time of an entire discharge. However, it never falls to zero and typically stays above 0.5%–1%. The reasons for such observed behavior will be investigated and discussed in the following sections.

Figure 3 also shows that the helium decay dynamics in the plasma and in the exhaust gas are similar. The two signals from the CXRS and the Penning gauge (when normalized) are overlapping within the CXRS error bars. This means that

equilibration between the plasma and the neutral gas (seen as separate He particle reservoirs) is faster than any other characteristic time describing helium exhaust. The resulting He compression, defined as the ratio between the two signals, is therefore constant during the discharges and is independent from the He content itself. The fact that the amount of helium present in the plasma does not affect the background plasma (at least in terms of divertor retention properties for helium) tells that for these shots, helium may be considered as a trace impurity. The measured compression values are shown at the top of figure 4. It increases roughly linearly with increasing divertor neutral pressure in the investigated range. This trend is in agreement with previous AUG studies with C wall and open [13] and closed [15] divertors. A one-by-one comparison between the past and current absolute numbers is, however, not meaningful. The divertor target geometry has changed, and the divertor retention is strongly dependent on geometric aspects, such as, e.g. target inclination and strike-point position [43].

In view of similar core confinement properties and equal pumping settings between the three discharges, the observed trend indicates a divertor retention of helium improving at higher divertor pressures. On the other hand, He enrichment (bottom plot of figure 4) is seen to decrease, also in qualitative agreement with previous studies. This indicates an increase in He dilution in the exhaust gas w.r.t. the main fuel, which is a detrimental effect in terms of extrapolation toward a reactor. The measured enrichment values for the investigated discharges are in the range 0.1–0.25, which is around the lower threshold limit quoted for the ITER design. Because of the opposite trends of the two parameters, an optimum point in divertor neutral pressure may be envisaged in view of reactor operations. Whereas helium pumping needs to be maximized, pumping of the main fuel will need to be carefully optimized. This comes from the competing needs of ensuring a good particle control and high plasma density and of minimizing the T throughput for safe operations of the fuel reprocessing plants [5, 9].





**Figure 3.** Time traces of the measured average He ion density in the core plasma by the CXRS (top) and He neutral atom density in front of the pumps (bottom) in the performed discharges at different divertor neutral pressures. Error bars of the CXRS data are given as shaded areas. The time windows during which helium is actively injected are highlighted by gray bands. The applied He fueling rates are also indicated. For discharge #39149, He ion density and He neutral atom density (the latter scaled and depicted as dotted) are overlapped to highlight the identical dynamic behavior between plasma and exhaust gas.

The estimated values of an effective He confinement time  $\tau_{\text{He}}^*$ , calculated through the model described later in the text, lie in the range 1.5–3.5 s for the shots here documented. This, combined with a measured energy confinement time of about 50 ms, leads to values of He confinement ratio  $\rho_{\text{He}}^* \equiv \tau_{\text{He}}^*/\tau_E$  [1] in the range of 30–70. These values are well above the conservative threshold of  $\rho_{\text{He}}^* = 5$ –10 estimated to avoid fuel dilution in a fusion reactor [5] and representative of the poor pumping capability of AUG w.r.t. helium.

#### 2.4. Helium exhaust and divertor detachment

A second series of experiments was aimed to investigate the impact of divertor detachment on helium exhaust. Previous studies reported a general detrimental effect on the exhaust efficiency of the divertor when entering a detached regime, manifested in a decrease in He compression [15].

We performed two discharges with constant D fueling; we applied strong N seeding to one of these discharges to actively cool the divertor plasma through enhanced radiation [44]. Figure 5 shows the main time traces and the relative Langmuir probe measurements.

The strong N seeding in the second discharge resulted in a pronounced detachment characterized by a cold divertor, with electron temperatures in front of the outer divertor target being  $<2$  eV as measured by Langmuir probes. In both discharges, we applied the same 300 ms long He puff from a midplane fueling valve.

Figure 6 shows the measured average He ion density in the core plasma. Regarding the Penning gauge measurements, in the discharge with the detached divertor, the strong presence of nitrogen generates additional emission lines in the neighborhood of the observed HeI line. This made the interpretation of the measured HeI line intensities problematic, and hence, any estimate of the He partial pressure is not reliable. Therefore, we do not report partial pressure measurements for these shots.

A qualitative interpretation of the time traces of the He ion content in the plasma can still be performed. The He ion density in the plasma decays visibly slower, after the active injection phase, with the cold/detached divertor. This reproduces the behavior observed in the full-C AUG and indicates a degradation of the exhaust efficiency with divertor detachment, which is presumably accompanied by a decrease of He compression in the divertor [15].

We also note that in the second discharge, as soon as N seeding starts (at 2.5 s), the He content in the plasma increases, proportionally to the N content, although no active injection is performed yet. An increase in the total He content in the exhaust gas was observed as well, although not quantifiable for the aforementioned reasons. This indicates a *net increase* of the He content in the entire system. In addition to the divertor detachment state, the presence of nitrogen also affects the confinement properties (e.g. increasing the edge-localized mode (ELM) frequency [45]) and may affect how efficiently the already-present helium is flushed away from the core [46]. This would justify a redistribution of the already-present helium between plasma and gas, which is indeed expected

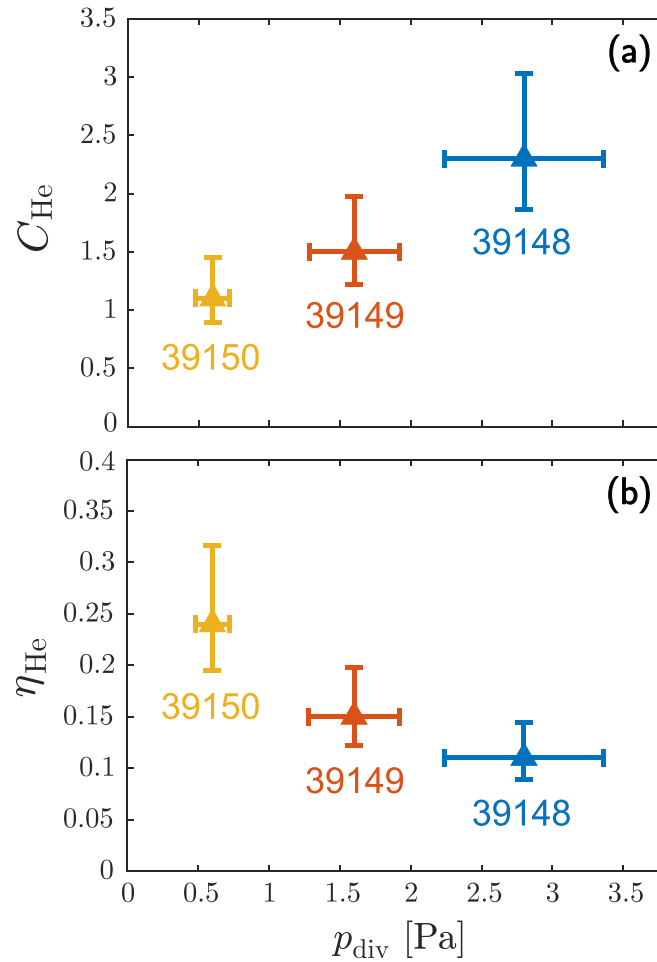


**Figure 4.** Measured values for (a) He compression (equation (1)) and (b) He enrichment (equation (2)) for discharges #39148, #39149, and #39150 as a function of the divertor neutral pressure.

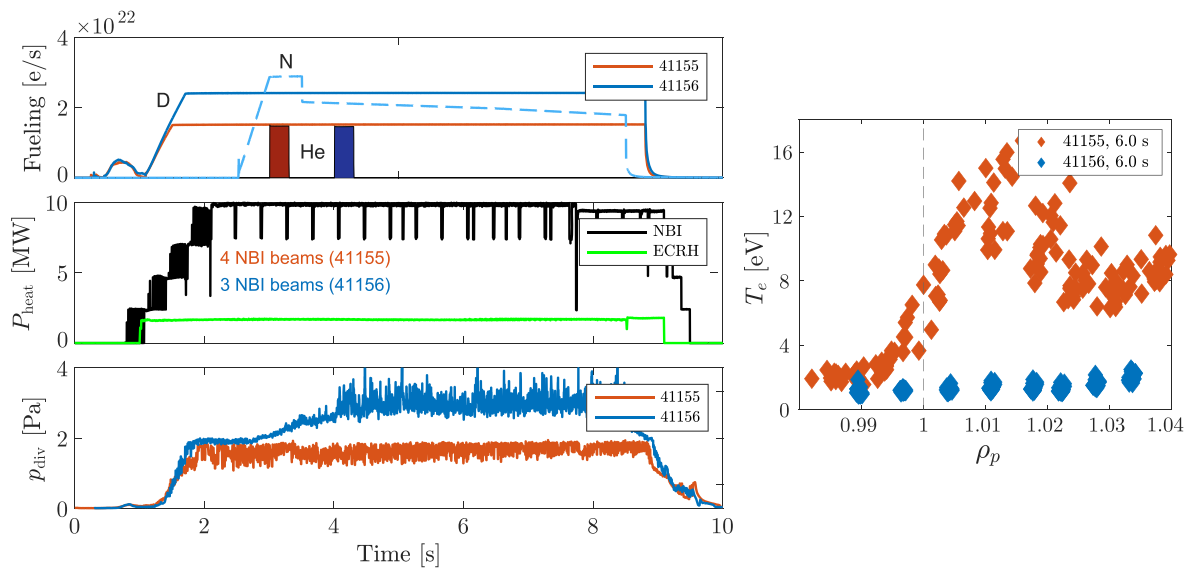


**Figure 5.** Left: some time traces from the performed divertor detachment scan. From top to bottom: fueling (D as solid lines, N as dashed lines (only for #41156), and He as filled areas, with the last one magnified four times w.r.t. the actual value), heating power (ECRH common for all the discharges; NBI with different numbers of beams), and divertor pressure (where the latter may be overestimated in the phase with active N seeding in #41156). Right: electron temperature profiles at the outer target surface measured by Langmuir probes.

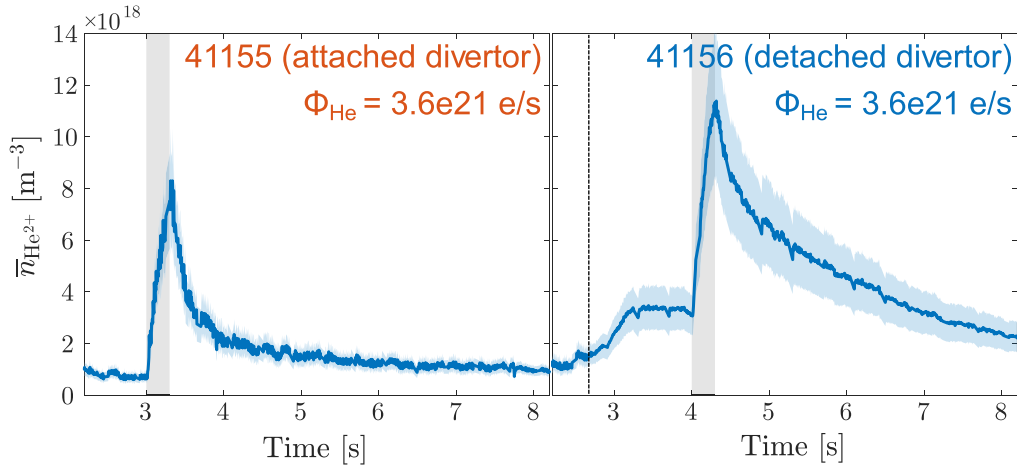


**Figure 6.** Time traces for the measured average He ion density in the core plasma by the CXRS in the performed discharges at different divertor detachment states. Error bars of the CXRS data are given as shaded areas. The time windows during which helium is actively injected are highlighted by gray bands. The applied He fueling rates are also indicated. The time at which N seeding starts in #41156 is indicated by a vertical dashed line.

[15], but not a net increase in the total amount of helium in the system. As we will motivate in the following sections, within the framework of the performed numerical modeling, an additional wall source may be invoked to explain this behavior.

### 3. Mechanisms for divertor retention of helium

In this section, we discuss the physical mechanisms governing helium divertor retention in the investigated discharges, and hence the resulting He compression, following the theoretical considerations presented, e.g. in [47–49]. Accordingly, the most important players are the main ion plasma flow in the divertor, the He ion flow pattern, and the ionization front of recycled He atoms.

The increase in He compression with divertor neutral pressure is likely to be attributed to the enhanced friction exerted by the increased recirculating ion flow of the main plasma species in front of the divertor targets [13]. The divertor neutral pressure is indeed closely linked to the level of main ion recycling from the divertor targets, at least in a tokamak like AUG, where the externally fueled flux of the main species is one to two orders of magnitude smaller than the recycled flux. This makes the divertor retention for helium, at AUG, insensitive to the external main particle fueling [40].

Although a reliable measurement of He compression with a detached/cold divertor was not available, the slower removal rate is sufficient to indicate a degraded helium divertor retention. A decrease of the removal rate, with identical pumping capability, is necessarily accompanied by a smaller He partial pressure in the divertor. This behavior is likely to be governed by (a) dependence of the stagnation point of the He ion flow along the near SOL and (b) variation of the mean free path of recycled He neutrals into the divertor plasma, both as functions of the divertor plasma temperature. The recycled He neutrals do not leak toward upstream only as long as they are ionized before the stagnation point of the He ion flow (case (1)

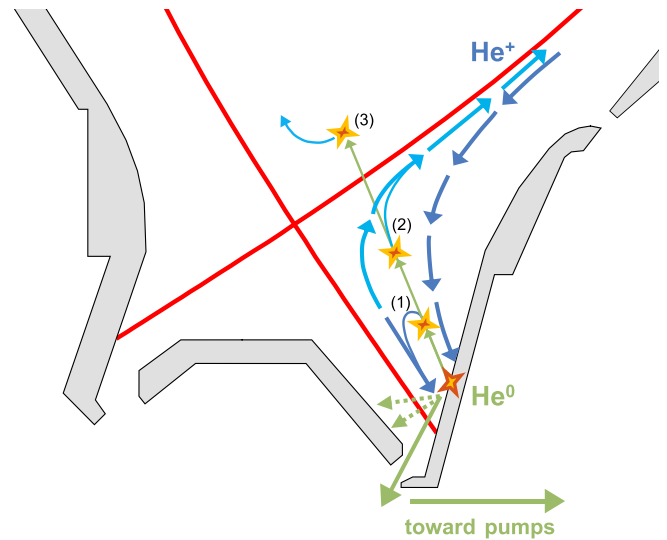


**Figure 7.** Helium recycling mechanisms governing divertor retention. (1) Attached/hot divertor: recycled He atoms are mostly ionized below the stagnation point of the He ion flow and promptly return to the divertor. (2) Detached/cold divertor: recycled He atoms are mostly ionized above the stagnation point and leak toward upstream following the ion flow reversal. (3) Extremely cold divertor: recycled He atoms fully penetrate the divertor plasma and reenter the confined region.

in figure 7). What happens with decreasing divertor temperature is as follows [47]:

- The friction on He ions exerted by the main ion flow decreases, even if the parallel  $D^+$  flux is the same, because the friction coefficient is inversely proportional to the ion temperature. Thermal forces toward upstream increase because of the more pronounced temperature gradient between upstream and divertor. Both these effects contribute to shift the He stagnation point toward upstream.



- The ionization front of recycled He atoms is also moved upstream because of the longer ionization mean free path in a colder divertor plasma.

These two mechanisms are in competition. However, SOLPS modeling of detached AUG plasmas has shown that for both nitrogen and argon, the shift upward of the impurity ionization front generally prevails [50, 51]. This results in recycled impurity neutrals being ionized above their stagnation point, and therefore, the impurity retention in the divertor region is reduced (case (2) in figure 7). The first ionization energy of helium (24.6 eV) is much larger than those of nitrogen (14.5 eV) and argon (15.8 eV). Therefore, the helium ionization mean free path in the divertor plasma is longer than for nitrogen and argon. The described mechanism may likely be then even more relevant for helium, resulting in a stronger detrimental dependence of divertor retention with decreasing divertor temperature than the one observed for nitrogen and argon. It cannot be excluded that, in the case of pronounced/-complete detachment, the divertor plasma is so cold that it becomes completely transparent for the recycled He neutrals. In this case, these would fully penetrate toward the confined region, regardless of the stagnation point of the He ion flow in the SOL (case (3) in figure 7).

These simplified considerations do not, however, include the effect of CX collisions between main ions and recycled impurity neutrals in the divertor region. Since CX reactions are effective at low plasma temperatures, the simple picture of an ionization-governed penetration depth of impurity neutrals, which increases with the colder divertor, may not be valid anymore.

A further ingredient determining the improvement of divertor retention with increasing neutral pressure might be a drag effect exerted on the neutral He flow by the D flow, given by D–He atomic collisions. The D neutral flow is indeed much more intense than the He flow because of the higher D neutral density and the additional sink provided by the cryopump. Consequent friction effects in the exhaust gas are then to be expected; given the dimensions of the AUG divertor and pumping ducts, the assumption of free molecular flow (Knudsen number  $\gtrsim 0.5$ ) would require pressures not larger than about 0.1 Pa, while for most H-mode AUG plasmas this threshold is surpassed (see figure 2). However, how much D–He friction does affect divertor retention of helium and sub-divertor helium gas transport is quantitatively unknown.

A more accurate quantification of these statements will be provided in a future publication, in which SOLPS simulations at different divertor pressures/temperatures of He-seeded AUG plasmas will be analyzed, and the possible impact of CX collisions in the divertor plasma and neutral–neutral collisions will be assessed.

#### 4. Model development for exhaust dynamics interpretation

Whereas divertor retention of recycled impurities is mostly dependent on the divertor plasma characteristics (e.g. pressure

and temperature), the exhaust dynamics is governed by the technical characteristics of one particular machine (e.g. wall materials and pumping system).

In the case of helium in AUG discharges, with pulse lengths up to 10 s, its exhaust is thought to be dominated by the wall, which acts as a continuous source and sink of He particles for the plasma. This occurs because helium is very efficiently retained into tungsten, resulting in a very high storage capacity of the main and divertor wall surfaces [26]. Therefore, in He-seeded plasmas, the time of a discharge may not be sufficient for saturating the wall with helium and ensuring a puff–pump balance. This is different from what happens with deuterium, for which a puff–pump balance is usually reached within 1 s in typical H-mode plasmas [52].

Understanding how the walls affect the transient behavior of externally injected impurities—including helium—is therefore necessary for a proper understanding of the global impurity life cycle in the plasma, from injection to permanent pumping. Studying and interpreting the exhaust dynamics can help to shed light on the mechanisms defining such a behavior. This is also useful for properly designing discharges in current devices with active impurity seeding for physics studies. Since accurate measurements of implantation and outflux of particles into/from the material walls during plasma discharges are challenging, such understanding must rely on the application of numerical models, which take into account the underlying plasma–wall interaction mechanisms.

##### 4.1. Coupling plasma transport and wall retention

Several transport codes (e.g. STRAHL [53] and DIVIMP [54]) have been developed for simulating the time-dependent impurity behavior in tokamak plasmas. Other than for transport studies, such codes have also been used in combination with wall retention models [55]. In dynamic wall composition and impurity migration studies, the simulated impurity fluxes toward the PFCs are e.g. used to calculate a dynamic impurity retention profile in the wall surface layers, in combination with a model for implantation/erosion processes [56–58]. However, how the dynamic absorption/release rates from the wall act as a dynamic sink/source for the impurity population in the plasma itself has never been taken into account.

For the first time, we develop a framework that accounts for time-dependent impurity transport in the plasma and wall retention in a self-consistent way, also including a simple model for neutrals recycling and pumping. This is in the form of a particle balance model, which simulates a series of interconnected particle reservoirs for ions, neutrals, and particles dynamically retained into the wall surfaces. The presented model is specifically adapted to the AUG geometry but can be easily generalized to any divertor tokamaks. We developed this as an extension of the 1.5D impurity transport code Aurora [59], which is a recent open-source code widely based on STRAHL. Aurora simulations are run with a high-level Python interface; the plasma/neutrals transport equations and the wall retention calculations are efficiently solved in Fortran routines. In this study, we only consider the case of helium in a machine with a full-tungsten wall. This model may be easily

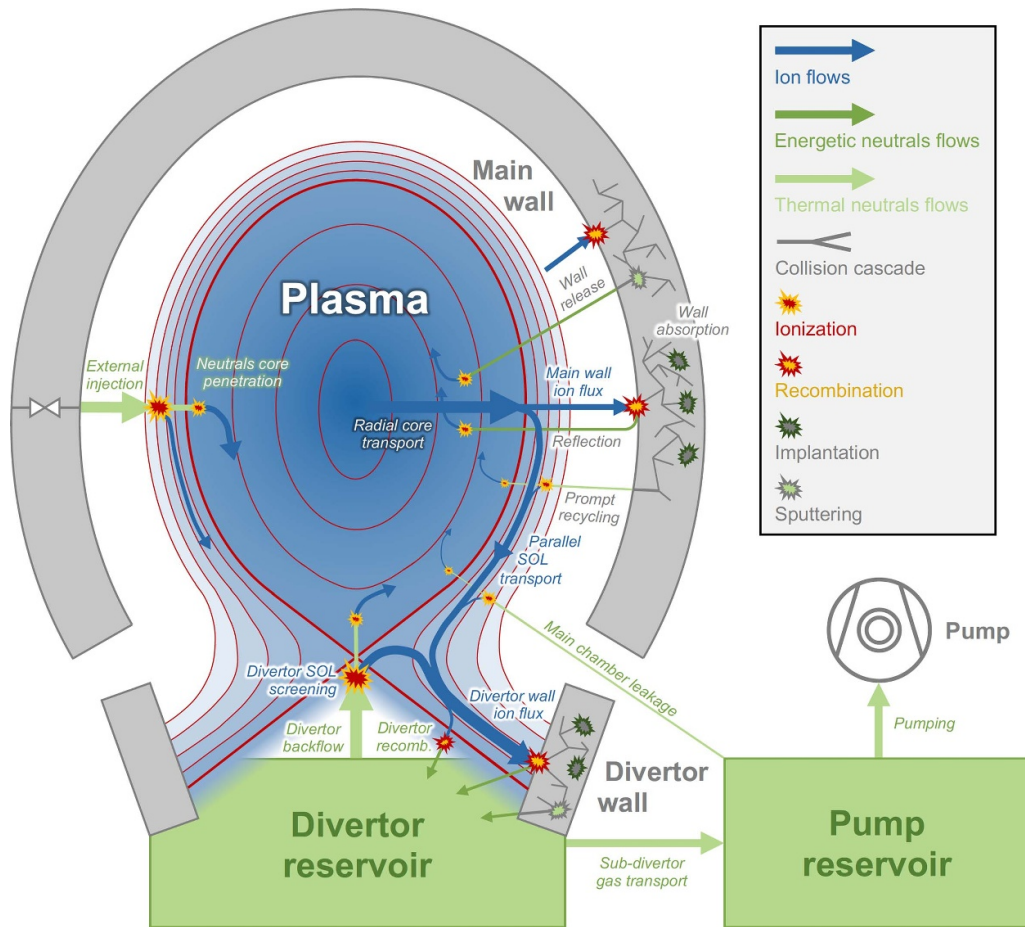


**Figure 8.** Sketch of the multi-reservoir particle balance model employed for the dynamic impurity transport modeling presented in this work. The plasma reservoir is assumed to be filled only with impurity ions. The divertor reservoir and the pump reservoir are assumed to be filled only with impurity neutrals. The main wall and divertor wall constitute reservoirs for long-term storage of impurity particles. The modeled interconnections are inspired by the actual AUG geometry, as the reader may note by comparing this sketch with figure 1.

generalized for any combination of impurity and wall material, provided that the relative plasma–wall interaction coefficients are calculated.

Here, we provide a brief description of the model. The plasma impurity transport model involves solving continuity equations for each charge state over time onto a 1D radial coordinate, assuming flux-surface-averaged quantities in a cylindrical geometry. Particle fluxes reaching the main and divertor walls can become stored on the wall surfaces (constituting 0D dynamic particle reservoirs) or be recycled. Particles leaving the main wall become a source for the plasma, while particles leaving the divertor wall fill further 0D dynamic neutral particle reservoirs resembling the divertor/pump chambers. From here, particles can flow back toward the plasma or be permanently removed from the system through pumping.

Figure 8 visually presents how the various particle reservoirs in our models are interconnected, as well as the included particle flows and physical processes.

**4.1.1. Impurity particle transport in the confined plasma.** 1D impurity ion transport modeling in the plasma reservoir is performed on a radial grid based upon the experimental magnetic

equilibrium. For each ion charge state, a continuity equation is solved, with radial (cross-field) particle flux computed assuming separate diffusive and convective components. Transitions between charge states are computed assuming ionization equilibrium. Outside the LCFS, an additional loss term is added, which emulates the particles lost due to parallel transport. For further details about the impurity ion transport model, we refer to [59].

**4.1.2. Plasma–wall interaction model.** The total parallel particle loss rate in the SOL constitutes the impurity flux reaching the divertor wall  $\Gamma_{\text{div}}$ . Instead, the radial particle flux at the outer grid boundary constitutes the impurity flux reaching the main wall  $\Gamma_{\text{main}}$ .

Impurity particle fluxes reaching the main and divertor walls fill up the dynamic particle reservoirs. Their content is expressed in terms of impurity particle surface densities  $\sigma_{\text{imp}}$  (in  $\text{m}^{-2}$ ), evaluated by dividing the total number of stored impurity particles by the user-defined wall surfaces.

A fraction of the impurities reaching the wall surface is reflected, according to the particle reflection coefficient  $R_{N,\text{imp}}$ . In this case, they are immediately reemitted, generally as fast

particles, carrying a relevant fraction of the original energy of the ion projectiles.

The fraction of the impurity flux, which is not reflected, may penetrate the wall surface. A saturation effect is included, considering a maximum particle surface density  $\sigma_{\text{imp,wall}}^{\text{sat}}$  [26]. The fraction  $\frac{\sigma_{\text{imp,wall}}}{\sigma_{\text{imp,wall}}^{\text{sat}}}$  of the nonreflected flux will be promptly reemitted as thermal neutrals. Only the remaining fraction  $(1 - \frac{\sigma_{\text{imp,wall}}}{\sigma_{\text{imp,wall}}^{\text{sat}}})$  will fill the wall reservoir, defining an *implanted impurity flux*

$$\Gamma_{\text{imp,wall}}^{\text{impl}} = \Gamma_{\text{imp,wall}} (1 - R_{N,\text{imp}}) \left( 1 - \frac{\sigma_{\text{imp,wall}}}{\sigma_{\text{imp,wall}}^{\text{sat}}} \right). \quad (4)$$

Once in the wall reservoirs, particles are stuck. However, they can be released again due to sputtering through ion bombardment of the wall surfaces. The projectiles doing this are not only those of the simulated impurity itself but also those of all the other species in the plasma, including the main species and possibly other impurity species. Therefore, the wall fluxes of the species not included in the current simulation need to be defined by the user. In this way, the *sputtered impurity flux* leaving the wall surface will be

$$\Gamma_{\text{imp,wall}}^{\text{sput}} = \sum_{\text{species}} Y_{\text{imp}}^s \Gamma_{s,\text{wall}}. \quad (5)$$

$Y_{\text{imp}}^s$  is a sputtering yield of the simulated impurity implanted on the wall surface caused by bombardment of the projectile  $s$ . These neutrals are also fast, carrying some fraction of the original energy of the ion projectiles.

The total recycled flux from the main wall and the energy at which the recycled impurity atoms are emitted allow us to estimate a neutral impurity density profile on the radial grid. This also allows us to roughly estimate how far each neutral population can penetrate into the confined plasma before being ionized.

**4.1.3. Neutrals recycling and pumping.** Impurity particles recycled from the divertor wall (reflected, promptly recycled, or sputtered) fill a dynamic particle reservoir of neutral particles, the *divertor reservoir*. The content of this reservoir is expressed in terms of volume density  $n_{0,\text{imp}}$  (in  $\text{m}^{-3}$ ), evaluated by dividing the total number of contained impurity particles by the user-defined reservoir volume.

Divertor retention (to be considered as an input for such a model) is emulated through a loss term for particles from the divertor reservoir, over a timescale given by an empirical divertor retention time  $\tau_{\text{ret}}$ . This defines a backflow of particles toward the plasma as

$$\Gamma_{\text{imp}}^{\text{back}} = \frac{N_{0,\text{imp}}^{\text{div}}}{\tau_{\text{ret}}} \quad (6)$$

where  $N_{0,\text{imp}} = n_{0,\text{imp}}^{\text{div}} V_{\text{div}}$ . A screening effect for the divertor may be optionally included, empirically defining the fraction of the total backflow, which gets to penetrate the divertor and to become a new source for the plasma.

The divertor reservoir is connected with a further *pump reservoir*. Neutral particle transport is defined through a neutral transport conductance  $L$ , in  $\text{m}^3 \text{s}^{-1}$ , such that the neutral flow from the divertor toward the pump is given by

$$\Gamma_{\text{imp}}^{\text{div-pump}} = L \left( n_{0,\text{imp}}^{\text{div}} - n_{0,\text{imp}}^{\text{pump}} \right). \quad (7)$$

$L$  can be empirically imposed to reproduce the experimental pressure/density drop between the divertor and the pump reservoirs.

Finally, particles in the pump reservoir can leak again toward the plasma, with a user-imposed leak conductance  $L_{\text{leak}}$  (although this possibility has not been exploited in the presented results), or they can be permanently removed from the system through active pumping. The pumped flux is

$$\Gamma_{\text{imp}}^{\text{out}} = S_{\text{pump}} n_{0,\text{imp}}^{\text{pump}} \quad (8)$$

with  $S_{\text{pump}}$  being the engineering pumping speed, in  $\text{m}^3 \text{s}^{-1}$ .

## 4.2. Physics input parameters

The developed model contains a large number of input parameters based on the experiment. Here follows a short description of the most important ones.

**4.2.1. Geometry.** According to the experimental equilibrium, the distance between LCFS and limiter shadow is 6 cm, while we set the distance between LCFS and grid boundary to 10 cm. We set the parallel connection lengths in the SOL to 50 m for the divertor SOL and to 1 m for the limiter SOL [60]. These are consistent with the magnetic equilibrium employed in the modeled discharges.

We set the surface areas for the main and divertor walls, used in the plasma-wall interaction calculations, to 5 and 0.5  $\text{m}^2$ , respectively, resembling the experimental plasma-wetted areas. Finally, we set the volumes for the divertor and pump reservoirs, used in the neutral transport calculations, to 0.8 and 1.7  $\text{m}^3$ , respectively, resembling the measured dimensions of the relative chambers within the AUG vacuum vessel.

**4.2.2. Transport coefficients.** The cross-field transport coefficients  $D_{\text{He}}$  and  $\nu_{\text{He}}$  and the parallel SOL flow velocity  $v_{\parallel,\text{He}}$  are the main input parameters for the ion impurity transport modeling.

In H-mode plasmas at AUG, it has usually been observed that helium transport in the core plasma is dominated by turbulence, with values of the particle diffusivity of a few  $\text{m}^2 \text{s}^{-1}$ , aside from the presence of possible internal transport barriers [28, 61]. Within the edge transport barrier (ETB), however, helium transport between ELMs is mostly collisional and well described by the neoclassical theory [46].

Figure 9 shows the employed particle diffusivity and convective velocity profiles for one modeled discharge (#39149), as red lines, and the resulting modeled  $\text{He}^{2+}$  density profile in the plasma. Inside the ETB, we set the values of  $D_{\text{He}}$  and  $\nu_{\text{He}}$  to reproduce the core CXRS data. In the framework of

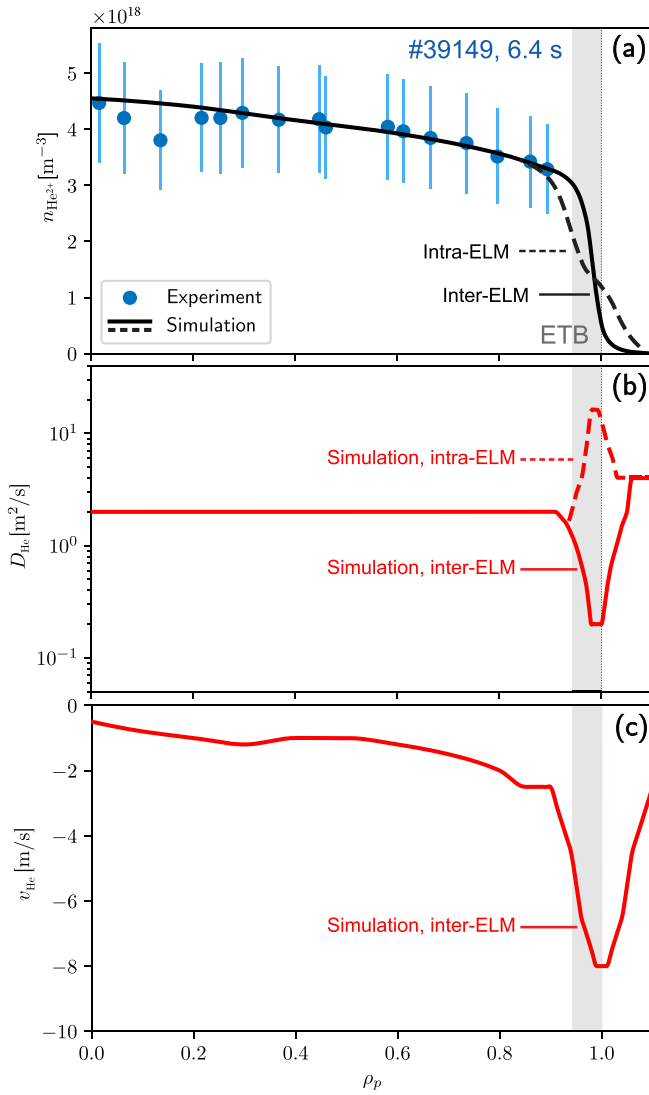


**Figure 9.** Radial profiles for (a) modeled He ion density profile (solid line, inter-ELM; dashed line, 1 ms after ELM crash) vs experimental CXRS data (blue points), (b) particle diffusivity  $D_{\text{He}}$ , and (c) convective velocity  $v_{\text{He}}$ . The solid red lines in (b) and (c) depict the coefficients used for the inter-ELM transport modeling. The dashed red line in (b) shows a periodically imposed increase in  $D_{\text{He}}$  to emulate the ELM crashes. The employed values for the inter-ELM transport coefficients in the performed modeling to reproduce the experimental CXRS core profiles are highly anomalous in the inner core, in agreement with previous studies [28]. Within the ETB, where no CXRS data were available, neoclassical values for both particle diffusivity and convective velocity were imposed [46], calculated using the FACIT program [62].

the presented modeling, the choice of specific values for  $D_{\text{He}}$  and  $v_{\text{He}}$  separately for the core is arbitrary, as what plays a role is only the ratio  $v_{\text{He}}/D_{\text{He}}$ . Within the ETB, instead, we set the values for  $D_{\text{He}}$  and  $v_{\text{He}}$  according to the neoclassical theory. This predicts, for helium, a radial transport mostly in the Pfirsch–Schlüter regime, with a strong inward directed convective velocity around the separatrix. No edge CXRS data for helium were available for the investigated discharges for comparison with the simulated He pedestal profile. However,

the simulated ratio of He ion densities between the pedestal top and the pedestal bottom of about 4–5 (solid black line in figure 9(a)) is compatible with already-published results analyzing the inter-ELM impurity pedestal profiles at AUG in similar plasma scenarios [63]. Outside the LCFS,  $D_{\text{He}}$  is raised to a second plateau [60], while  $v_{\text{He}}$  is reduced symmetrically w.r.t. the separatrix location [46]. In the absence of solid information about helium transport outside the LCFS, we chose the value for  $D_{\text{He}}$  here to achieve a decay length of the He ion density profile in the SOL comparable with that of the electron density.

We also implemented a time-dependent parametrization of the transport coefficients to emulate the ELM events. ELMs contribute to boost the ejection of impurities from the core plasma [46]. Therefore, a periodic increase in edge transport must be accounted for a correct core confinement modeling. The inclusion of ELMs is inspired by [60]. The transport is modulated with a sudden increase of  $D_{\text{He}}$  up to values of the order of  $10\text{--}20\text{ m}^2\text{ s}^{-1}$  at the edge to emulate the ELM crash. After that, it decays linearly within 1.2 ms back to the neoclassical value and remains constant until the successive ELM event. This is done with a frequency consistent with the experimental one (which is within the range 125–200 Hz for the investigated discharges). In this way, the achieved flattening of the modeled He profile during ELM events at the edge (dashed black line in figure 9(a)) is also compatible with previously analyzed experimental intra-ELM profiles [63].

Finally, for the specification of the parallel ion flow velocity describing the parallel losses outside the LCFS, we assumed that, in the experiment, the He ion flow is fully entrained into the D ion flow [60]. This is reasonable, as the collisional mean free path between the D and He ions is within the range 0.1–1 m at usual AUG SOL plasma conditions ( $n_e \approx 2\text{--}3 \times 10^{19}\text{ m}^{-3}$ ,  $T_e \approx 50\text{--}100\text{ eV}$ ), assuming  $n_{\text{He}^{2+}} \approx 0.1 n_{\text{D}^+}$ , i.e. much shorter than the parallel connection length. We then specified the He flow velocity as  $v_{\parallel, \text{He}} \approx v_{\parallel, \text{D}} = M \sqrt{(3T_i + T_e)/m_{\text{D}}}$ . The employed Mach number  $M$  was within the range 0.1–0.3.

**4.2.3. Kinetic profiles and atomic rates.** We took the kinetic profiles of the background plasma from the experiment. This allows the specification, after the assumption of coronal equilibrium, of the atomic rates used for the calculation of the ion sources/sinks for every charge stage of helium.

Figure 10 shows the employed kinetic profiles for the discharge #39149 and the resulting He atomic rates used in the transport calculations, obtained from the ADAS data [34]. For the electron density and temperature, we used a fit achieved through an integrated data analysis [64]. This is derived from a Bayesian probabilistic analysis, including the measurements of different diagnostics, which include lithium-beam emission spectroscopy [65], vertical Thomson scattering [66], and electron cyclotron emission radiometry [67]. For the ion temperature, we used a spline fit to core and edge CXRS data [68].

**4.2.4. Wall loads and surface coefficients.** Modeling the plasma–wall interaction, which is necessary for simulating wall retention, requires the knowledge of reflection



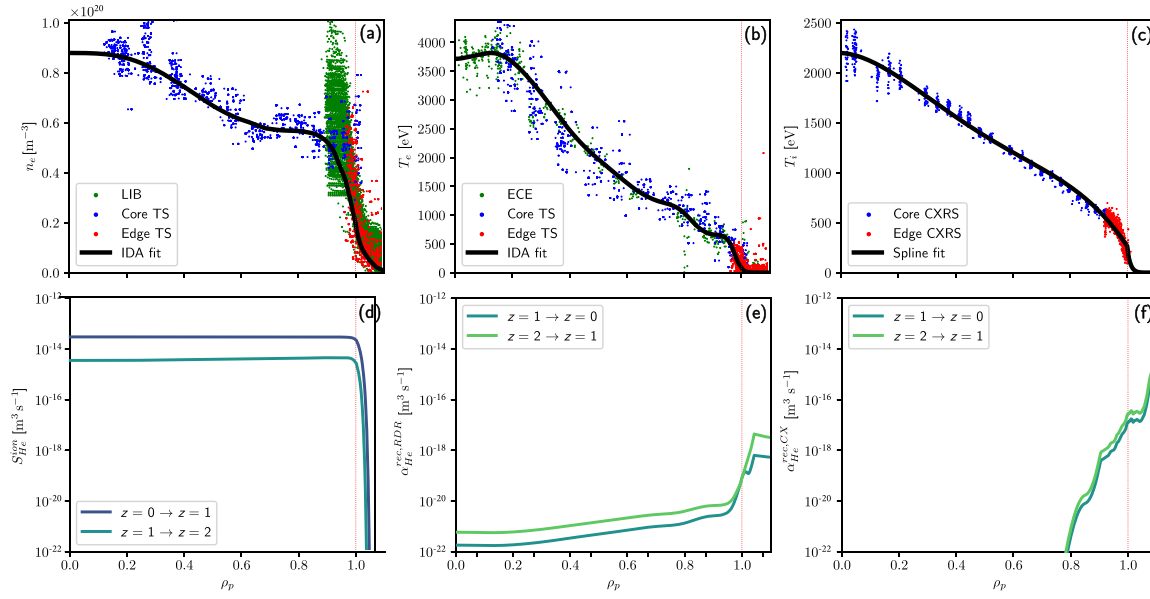


**Figure 10.** Top row: experimental data on (a) electron density, (b) electron temperature, and (c) ion temperature at the plasma midplane, taken from different diagnostics, as colored points. The employed fitted profiles for calculating the He atomic rates are given by black lines. All the data refer to the AUG discharge #39149 within the time window [2.5; 3.0] s. Bottom row: calculated He atomic rates for all the charge transitions, namely (d) ionization rates, (e) radiative + dielectric recombination rates, and (f) CX-assisted recombination rates, extracted from the ADF11 ADAS database.

coefficients and sputtering yields for the considered ion/material species. Both types of data were calculated using the binary-collision-approximation-based Monte Carlo code TRIM.SP [69, 70]. We extracted the reflection coefficients for helium on tungsten, used in equation (4), from an already-published database [71]. We calculated instead the sputtering yields for helium implanted in tungsten, used in equation (5), for the purpose of this work. Figure 11 shows the employed coefficients. All surface coefficients are dependent on the impact angle of the ion projectiles onto the surfaces. For the data reported in figure 11 and used in our modeling, we assume the impact angle of all considered species of about  $65^\circ$ . This is a good assumption for light projectiles (for which long-range transport prevails over prompt redeposition) derived from gyro-orbit calculations, considering AUG-typical magnetic field intensity and inclination onto material surfaces, sheath characteristics, and wall roughness [72].

The particle reflection coefficient  $R_{N,\text{He}}$  for helium on tungsten (figure 11(a)) is used to calculate the reflected He flux from the wall surfaces, as a function of the projectile impact energy, as

$$\Gamma_{\text{He,refl}} = R_{N,\text{He}} \cdot \Gamma_{\text{He,wall}}. \quad (9)$$

The mean energy of the reflected He atoms from tungsten (figure 11(b)) is also specified as a function of the projectile impact energy  $E_{0,\text{He}}$ , as

$$\langle E_{\text{He,refl}} \rangle = E_{0,\text{He}} \cdot \frac{R_{E,\text{He}}}{R_{N,\text{He}}} \quad (10)$$

with  $R_{E,\text{He}}$  energy reflection coefficient for helium on tungsten.

We obtained the curves for the particle/energy reflection coefficients used in this study (blue curves in the left plot in figure 11) from the Eckstein fit function formula:

$$R_{(N/E),\text{He}} = \frac{a_1 \epsilon^{a_2}}{1 + a_3 \epsilon^{a_4}} \quad (11)$$

with  $a_1, a_2, a_3, a_4$  fit coefficients, as a function of the reduced energy  $\epsilon \equiv E_0/E_{\text{TF}}$ .  $E_0$  is the assumed impact energy of He on W, and  $E_{\text{TF}} = 2.0376 \times 10^4$  eV is the Thomas–Fermi energy for helium impinging on tungsten.

For the calculation of the sputtering coefficients for helium implanted into tungsten, we assumed that He atoms uniformly implanted into a layer of surface material up to a given depth, with no surface binding energy to the bulk lattice atoms. We assumed the depth of the implantation profile to be equal to the mean penetration depths of He atoms into a W lattice, also calculated by TRIM.SP. Such depths are about 3 nm for the main wall and about 6 nm for the divertor wall. The difference between the calculated depths comes from the different average impact energies for helium on tungsten during plasma operations.

We calculated the sputtering yields for the same ion projectiles present in the experiments, i.e. in addition to helium itself, deuterium and nitrogen (figure 11(c)). Individual points refer to different assumed He atom concentrations within the W lattice ( $f_{\text{He}} \equiv N_{\text{He}}/(N_{\text{W}} + N_{\text{He}})$ ). The normalized yields, i.e.  $Y_{\text{He}}/f_{\text{He}}$ , have been fitted (bluish curves) with a single fit function formula defined by Bohdansky:

$$Y_{\text{He}}/f_{\text{He}} = Q \cdot S_n \cdot \left[ 1 - \left( \frac{E_{\text{th}}}{E_{0,s}} \right)^{2/3} \right] \cdot \left( 1 - \frac{E_{\text{th}}}{E_{0,s}} \right)^2 \quad (12)$$

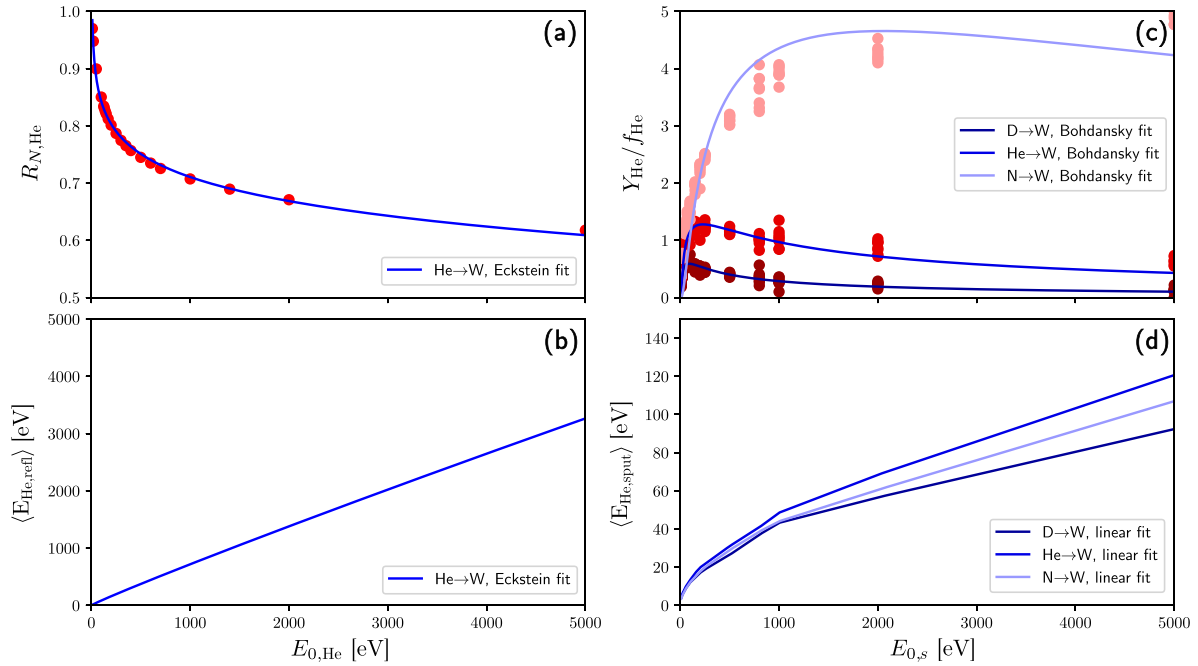


**Figure 11.** Surface coefficients employed for the plasma–wall interaction modeling as functions of projectile impact energy, assuming an impact angle of  $65^\circ$ . (a) Particle reflection coefficient (original data and fit function) and (b) mean reflection energy for He on W. (c) Normalized sputtering yields (original data and fit functions) and (d) mean sputtered energies for He implanted in W eroded by different projectiles (D, He, and N).

with  $Q$ ,  $E_{th}$  fit coefficients, as functions of the parameter  $S_n = [0.5 \cdot \ln(1 + 1.2288 \cdot \epsilon)] / [\epsilon + 0.1728 \cdot \sqrt{\epsilon} + 0.008 \cdot \epsilon^{0.1504}]$ , of the projectile energy  $E_{0,s}$ , and of  $\epsilon \equiv E_{0,s}/E_{TF}$ .

This allowed us to calculate the sputtered He flux, from the impinging projectile species  $s$ , as

$$\Gamma_{He,sput}^y = \frac{Y_{He}}{f_{He}} \cdot f_{He} \cdot \Gamma_{s,wall}. \quad (13)$$

We also calculated the mean energy  $\langle E_{He,sput} \rangle$  of the sputtered He atoms from tungsten (figure 11(d)) as a function of the projectile impact energy.

Different projectiles eroding He atoms implanted in tungsten behave in different ways. At impact energies of up to a few hundreds of electron volts, the normalized yields are comparable. At impact energies of up to a few thousands of electron volts (which may occur during ELMs [73]), a strong dependence on the eroding species arises, scaling with the mass of the projectiles. In this range, a given impinging flux of nitrogen is, e.g. up to 40 times more efficient than the same impinging flux of deuterium in eroding He atoms implanted in tungsten.

A correct application of the described surface coefficients requires to know:

- The mean impact energy of He ions onto the main and divertor wall surfaces, in order to choose the correct reflection coefficients and sputtering yields
- The total ion fluxes of the background plasma species (deuterium and nitrogen) onto the main and divertor wall

surfaces and relative mean impact energies, in order to calculate the sputtered He fluxes from the background species.

Consistent with the dynamic modeling of ELM-driven transport, we had to adapt such input parameters providing both inter- and intra-ELM values for wall fluxes of background species and mean impact energies. The imposed inter- and intra-ELM values for the background fluxes are consistent with the Langmuir probe measurements. We then derived the imposed inter- and intra-ELM values for the impact energies of both helium and background species as a function of the measured plasma parameters. The predicted values of inter-ELM impact energies for the considered species are within 100–200 eV for the main wall and within 200–400 eV for the divertor wall. Due to increased parallel energy transfer at the ELM peak, the predicted values of the intra-ELM impact energies may reach several thousands of electron volts. More details about the definition of wall loads as input parameters for the dynamic modeling are given in appendix A.

**4.2.5. Free parameters.** In addition to the just described input parameters coming directly from the experiment, the model features a number of inputs, which should be considered free parameters. Since the model effectively captures, albeit in a very simplified way, all mechanisms relevant to impurity transport, recycling, and pumping, a successful modeling may still be performed by imposing values for such free parameters to fit the available experimental measurements. An overview of the most relevant free input parameters is given in appendix B.



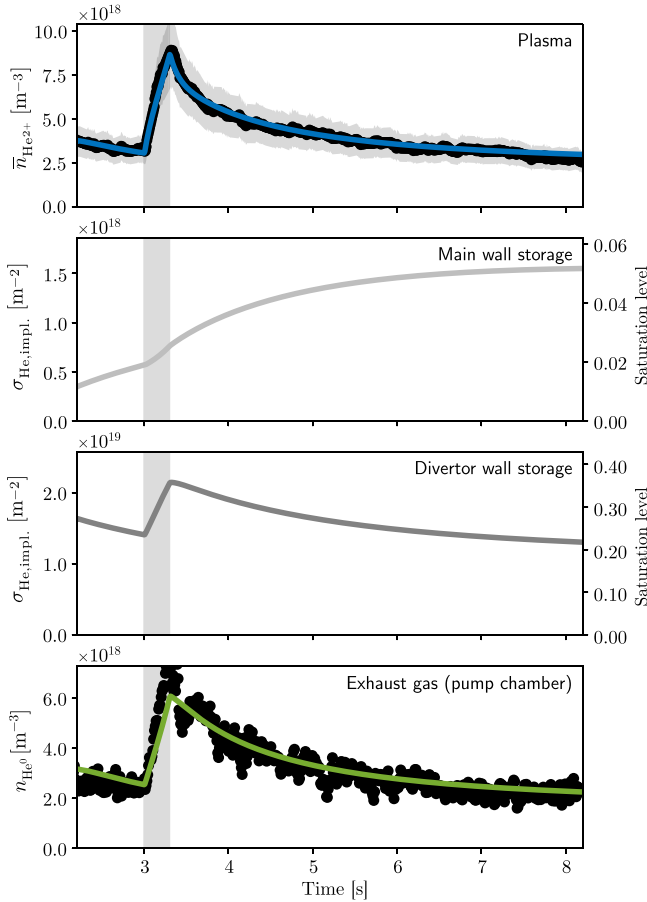


**Figure 12.** Modeled time traces of the He particle content in the reservoirs described in figure 8 for the discharge #39149. Top plot: average He ion density in the core plasma (equation (3)) and comparison with the CXRS measurements (black points). Middle plots: surface densities of He atoms dynamically retained at the main and divertor walls; these are also expressed in terms of saturation level, i.e. fraction between the dynamically implanted He atoms and the maximum number of He atoms that the walls can accommodate ( $\sigma_{\text{imp,wall}}/\sigma_{\text{imp,wall}}^{\text{sat}}$ ). Bottom plot: neutral He density in the pump reservoir and comparison with the Penning gauge measurements (black points).

## 5. Modeling results

We performed a number of time-dependent simulations of AUG discharges self-consistently coupling plasma impurity transport, neutrals recycling and pumping, and wall retention. The simulations cover the stationary phase in the investigated discharges. The plasma background remains constant in such a time window. This allows us to follow the behavior of helium as a trace impurity. The amount of helium already present in the system at the initial time of the simulations is set up in the form of initial conditions for the dynamic simulations.

Figure 12 shows an example of a time-dependent simulation for the AUG discharge #39149, which is one of those described in section 2.3, following the dynamic behavior of helium in the particle reservoirs described in figure 8. The simulations were performed with a constant time step of  $5 \times 10^{-5}$  s. The optimized routines used by Aurora keep the data into

dynamically allocated memory, rather than writing to disk [59]. This allows us to perform such simulations, comprising a number of time steps of the order of  $10^5$ , in less than 1 min on an ordinary personal computer.

With the imposed experimental parameters and a proper choice of several free parameters, which are described throughout the text, the model successfully reproduced the experimentally observed exhaust dynamics. The measured average He ion content in the confined plasma measured by CXRS (top plot in figure 12) and the neutral He density in the exhaust gas measured by the Penning gauge (bottom plot in figure 12) were matched before, during, and after the external He injection phase. The proper imposition of the transport coefficients also allowed the modeled He ion density profile in the core plasma to match the radially resolved CXRS measurements at each time (see, e.g. figure 9). We imposed the external source of He particles consistently with the experimental He puff, i.e. in the time window [3.0, 3.3] s with the intensity of  $1.25 \times 10^{21}$  injected He ions  $\text{s}^{-1}$ . The middle plots in figure 12 show the modeled number of He atoms dynamically retained at the main and divertor wall surfaces in terms of surface densities.

Unless specified, the plots of the reservoir contents presented in this section show temporal averages of the modeled time traces over ELM cycles, i.e. in the form

$$\langle n_{\text{He}} \rangle(t) = \frac{1}{\Delta t_{\text{ELM}}} \int_t^{t+\Delta t_{\text{ELM}}} n_{\text{He}}(t') dt' \quad (14)$$

where  $\Delta t_{\text{ELM}}$  is the duration of an ELM cycle.

All the simulations show a very satisfactory balance between injected particles, removed particles, and particles dynamically contained in the various reservoirs. The typical error in the numerical particle conservation is less than 1%.

### 5.1. Role of wall retention in the exhaust dynamics

**5.1.1. Global wall inventory balances.** The balance between absorption and release rates into/from the wall reservoirs is crucial for the achievement of a good match with the experimental measurements in the plasma and neutrals reservoirs. The main wall reservoir constantly acts as a net sink for He ions from the plasma, as the modeled number of implanted He atoms always increases throughout the discharge. The divertor wall reservoir instead acts as a net source of He atoms, as the modeled number of implanted He atoms decreases, apart from the time window of the external puff. This is made clear by showing the individual absorption and release rates for the main and divertor walls, referred to the discharge #39149 (left plots of figure 13). For the main wall, the absorption rate is always larger than the release rate. For the divertor wall, the release rate is slightly larger than the absorption rate, apart from the time window of the external puff.

Table 1 contains the modeled global particle balance for the main and divertor wall reservoirs integrated over the decay phase of discharge #39149, i.e. in the time window [3.3; 8.2] s. Globally, the main wall has absorbed  $2.46 \times 10^{20}$  He atoms, while the divertor wall has released  $2.69 \times 10^{20}$  He atoms.

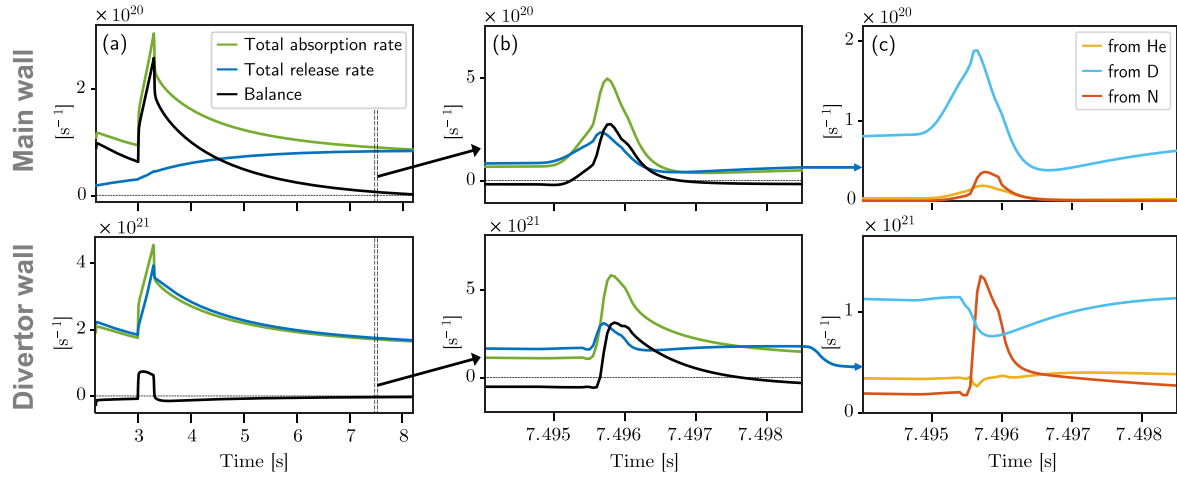


**Figure 13.** Modeled dynamic balances for the main and divertor walls for discharge #39149. From left to right: (a) individual ELM-averaged absorption and release rates governing the dynamic wall behavior; (b) zoom-in time of the absorption and release rates during an ELM event; (c) decomposition of the release rate during an ELM event in terms of eroding species.

**Table 1.** Modeled global balances for the main and divertor wall reservoirs for discharge #39149 during the decay phase (i.e. time window [3.3; 8.2] s). The global wall balances are given by the difference between the absorbed He atoms and the released He atoms within the considered time window. The decomposition of the total number of released He atoms in terms of eroding species is also shown.

	Main wall reservoir	Divertor wall reservoir
Initial content ( $t = 3.3$ s)	$2.39 \times 10^{20}$	$6.74 \times 10^{20}$
Final content ( $t = 8.2$ s)	$4.85 \times 10^{20}$	$4.05 \times 10^{20}$
Wall balance	$+2.46 \times 10^{20}$	$-2.69 \times 10^{20}$
Total absorbed He atoms	$6.01 \times 10^{20}$	$10.35 \times 10^{21}$
Total released He atoms	$3.55 \times 10^{20}$	$10.62 \times 10^{21}$
(Released by He sputtering)	$0.23 \times 10^{20}$ (6.5%)	$2.81 \times 10^{21}$ (26.5%)
(Released by D sputtering)	$3.18 \times 10^{20}$ (89.6%)	$6.11 \times 10^{21}$ (57.5%)
(Released by N sputtering)	$0.14 \times 10^{20}$ (3.9%)	$1.70 \times 10^{21}$ (16.0%)

We note that many more He atoms are exchanged (absorbed and released) with the divertor wall than with the main wall, although the divertor wall surface area is smaller than that of the main wall. This is not surprising, given the much higher ion fluxes reaching the divertor. It is also worth noting that the effect of the two walls combined (i.e. the net sum of the two wall balances) is only a moderate net release of He atoms toward the plasma when integrated within the full time window of the decay phase ([3.3; 8.2] s). What mostly contributes to slowing down the decay of the He content in the plasma is rather the fact that each He particle might undergo several absorption/release cycles from the walls before being permanently removed by active pumping.

**5.12. Saturation behavior of wall reservoirs.** The modeled saturation levels ( $\sigma_{\text{He,wall}}/\sigma_{\text{He,wall}}^{\text{sat}}$ ) are far below unity, especially for the main wall, in which this stays below 10% (see figure 12). The fact that the main wall is farther away from saturation w.r.t. the divertor wall determines the fact that the former constantly acts as a particle absorber. The elevated absorption capability of the two walls implies that, even in a situation of constant external He gas puff, wall saturation with

helium is hardly reachable within the time of a discharge. This is consistent with the experimental evidence of the He content in AUG plasmas never reaching a constant value when a constant puff is applied.

The employed values for the saturation density, which must be regarded as a free parameter for the model, are  $3 \times 10^{19} \text{ m}^{-2}$  for the main wall and  $6 \times 10^{19} \text{ m}^{-2}$  for the divertor wall. These were chosen after performing a sensitivity analysis on the impact of such parameters on the dynamic solutions (see appendix B, figure 16). A larger value assumed for the divertor wall reasonably comes from the higher average impact energies of He ions striking this, which may then penetrate more in depth into the material lattice. The chosen values are roughly consistent with past experimental observations. It was observed that W surfaces can accommodate up to  $5 \times 10^{19}$  He atoms per  $\text{m}^2$  when bombarded with 200 eV He beams, or up to  $10 \times 10^{19}$  He atoms per  $\text{m}^2$  when bombarded with 600 eV He beams [26]. These values are about one order of magnitude larger than what is observed for C surfaces. The efficient retention of He atoms in tungsten can then be invoked as a major player in explaining the well-detectable He content in AUG plasmas even in discharges without active He seeding [26],

w.r.t. that observed in the full-C AUG. This is consistent with the key role of the walls as particle reservoirs in this modeling.

**5.1.3. Inter- and intra-ELM plasma-wall interactions.** The middle plots of figure 13 show a zoomed-in excerpt of the same modeled absorption/release rates of the left plots but without temporal averaging over ELMs. This allows us to observe the modeled wall behavior over an ELM cycle. During ELMs, the sudden increase in wall fluxes results in a trivial increase of both implantation and sputtering rates. However, the increase in the implantation rates prevails over the increase in the sputtering rates for both the main and divertor walls. This means that the net effect of ELMs is a transient amplification of wall absorption of helium. This is in contrast to the effect of ELMs on the bulk wall materials, whose global release rate is seen to be amplified during ELMs [60].

The right plots of figure 13 show the decomposition of the sputtering rates in terms of eroding species. For the main wall, helium release is dominated by D sputtering both between and within ELMs. For the divertor wall, the sputtering components by impurities (He and N) are proportionally larger than for the main wall but still less relevant than D sputtering in inter-ELM phases. Within ELMs, we note a decrease in D sputtering and a strong increase in N sputtering. The latter component temporarily becomes the dominant one, although the imposed N flux toward the wall surface is much less than the imposed D flux. This is explained by the sputtering yield for helium released by D decreasing at impact energies of thousands of electron volts (assumed at the ELM peak); see figure 11. At the same energy, instead, the sputtering yield for helium released by N is much higher than at inter-ELM energies. See appendix A for the definition of the assumed wall fluxes and impact energies for the various species.

**5.1.4. Global He erosion sources by different sputtering species.** The global contribution of the various species when coming to eroding helium implanted within the walls can also be assessed. See appendix A for details about the D/N wall fluxes assumed for the simulations.

Globally (see table 1), the helium release from the main wall is dominated by D sputtering. Instead, for the divertor wall, which is the most relevant dynamic source of eroded He atoms, almost half of the released He atoms are due to impurity sputtering (He self-bombardment and N bombardment). N sputtering causes about 16% of the helium release from the divertor wall, although the N content in the modeled discharge is very moderate: the N fueling (in ions  $s^{-1}$ ) is indeed only 3% of D fueling. This translates into relatively small N ion fluxes toward the wall as input for the simulation (see figure 15). It may then be expected that in discharges with strong N fueling, N becomes the main eroding species for helium implanted in the walls. This is consistent with what is observed in discharge #41156, in which when the N fueling is ramped from 0% to 13% of D fueling (in ions  $s^{-1}$ ), the amount of helium present in the plasma roughly doubles (see figure 6). According to these numbers, such an additional amount of nitrogen would provide a new source of helium for the plasma, as a result of additional

wall erosion, of amount comparable with that already present from D erosion.

**5.1.5. Validity of the plasma-wall interaction calculations.** The presented results regarding implantation and erosion of helium into/from W surfaces are achieved through very simplified calculations and by means of several ad hoc assumptions.

Whereas in our model erosion due to ion bombardment is the sole mechanism allowing implanted impurity atoms to be released from the wall, in principle also outgassing due to thermal effusion may play a role because of the PFC temperatures reaching up to 1000 K during plasma discharges. He outgassing may be, in principle, estimated by measuring the He partial pressure in the exhaust gas immediately after the end of plasma discharges, when the wall surfaces are still hot (so thermal release is still comparable to that during the plasma phase). However, such measurement is very challenging: the employed Penning gauge does not operate anymore as soon as the magnetic field is terminated, and attempts to use conventional and high-resolution mass spectrometers for measuring the He partial pressure at AUG have been so far unsuccessful. We believe, however, that during plasma discharges, outgassing is much less relevant than erosion. This is supported by the dynamic behavior of helium in discharge #41156 after the start of N seeding (see figure 6): a more than double amount of helium in the plasma only after the start of N seeding clearly indicates that any release component due to erosion dominates over the release component due to outgassing (see also the discussion in section 5.1.4).

Additionally, when translating the imposed surface areas of the main and divertor walls into maximum absolute number of He atoms that these can accommodate, starting from the saturation densities, we had to use a multiplication factor. If we use the mere geometric plasma-wetted areas for the plasma-wall interaction calculations (i.e. 5 and 0.5  $m^2$  for the main and divertor walls, respectively), the resulting particle exchange between the plasma and wall surfaces would be not sufficient to reproduce the observed dynamics. A possible explanation of this is given by considering wall roughness. The employed reflection coefficients and sputtering yields were calculated by assuming polished W surfaces. Effective surface coefficients of rough surfaces might be much different than the ones of polished surfaces [74, 75]. Plasma-exposed W PFCs at AUG show a roughness of the order of several micrometers [76]. The implantation profile of helium retained into a W surface only extends to a depth of a few nanometers. It is therefore not surprising that accounting for wall roughness would imply increased effective surface areas, in which He atoms can be implanted when using surface coefficients calculated for polished surfaces. After a further sensitivity analysis (see appendix B, figure 16), we found that in order to match experimental and modeled dynamics, we had to multiply the plasma-wetted areas by a factor of 60. This implies a much larger absolute number of He atoms, which the wall can accommodate before saturating, still using the same values for the saturation densities, as suggested by experimental evidence [26]. Such multiplication factor, which we qualitatively motivate

by accounting for wall roughness, is just a fit parameter for our modeling and is not intended to have any precise physical meaning. We do not claim that roughness does really increase the effective surface area exposed to the plasma fluxes by a factor of 60. A figure of merit usually defining wall roughness in the literature is the vertical deviation of a surface topography from the mean height: how this relates to an effective surface area to be used for plasma–wall interaction calculation, when using coefficients calculated for polished surfaces, is difficult to quantify. Rather, the factor of 60 should be regarded as an arbitrary parameter, whose specification is required to fit the experimental measurements and model the global picture of how much helium is dynamically stored in the various particle reservoirs and of the particle exchange rates between plasma and walls. Any other statement about the wall morphology is beyond the scope of this work.

### 5.2. Impact of active pumping and wall pumping in determining the exhaust dynamics

A further feature of our multi-reservoir particle balance model is the possibility to disentangle the impact of long-term wall storage and inefficient pumping in determining the helium exhaust dynamics at AUG.

We performed a series of simulations, changing individual features one at a time:

- (1) Full simulation with realistic pumping speed ( $S_{\text{pump}} = 7 \text{ m}^3 \text{ s}^{-1}$ , i.e. considering only the effect of the AUG turbomolecular pumps) and with activated wall retention model
- (2) Simulation with realistic pumping speed but with a deactivated wall retention model (i.e. the wall is fully recycling)
- (3) Simulation with enhanced pumping speed ( $S_{\text{pump}} = 7 + 120 = 127 \text{ m}^3 \text{ s}^{-1}$ , i.e. assuming helium to be removed also by the AUG cryopump) but with an activated wall retention model
- (4) Simulation with enhanced pumping speed and with a deactivated wall retention model

Simulations were performed based on the AUG discharge #39149 starting at  $t = 3.3 \text{ s}$ , i.e. at the end of the active injection phase, in order to follow the He decay phase. Figure 14 shows the modeled decay curves. Table 2 shows the global particle conservation for the modeled time window, in units of absolute number of particles.

Helium removal becomes more efficient neglecting wall retention (simulation (2)) w.r.t. the full model (simulation (1)), albeit keeping the same pumping speed. This is explained by noting that He particles ‘pumped’ from the walls in simulation (1) are not permanently removed from the system, as they can be reinjected into the plasma. In simulation (2), we exclude the possibility for He particles to be temporarily retained in the wall reservoirs. Wall retention, in this sense, delays a permanent removal of He particles from the system, as these ‘spend’ some amount of time stuck at the walls.

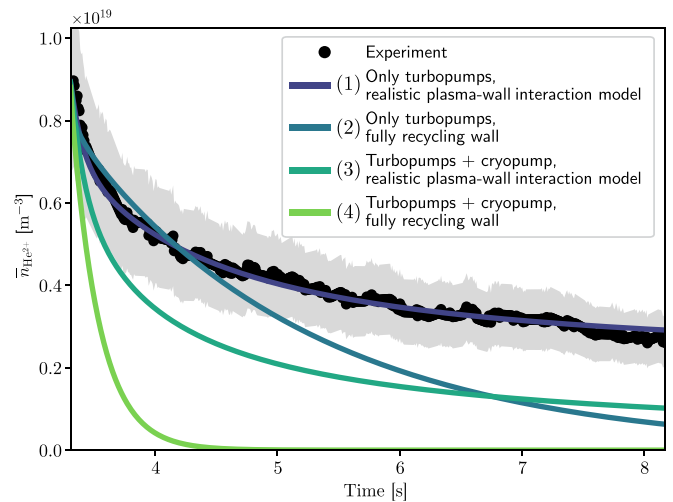


**Figure 14.** Modeled decay curves for the He content in the plasma for the four test simulations described in section 5.2. The simulations were performed with no external He source, same initial conditions, and same input parameters apart from wall and pump settings.

Enhancing only the pumping speed (simulation (3)), maintaining the wall retention model activated, we also note a trivial enhancement of helium exhaust w.r.t. the full model (simulation (1)). In this case, helium removal is still hindered by the possibility for He particles to spend time within the walls. Since the active removal is faster, however, He particles have less time to interact with the wall (and hence be absorbed).

In simulations (2) and (3), the final He content in the modeled time window is similar. Therefore, we conclude that wall retention and inefficient pumping individually play a similar quantitative role in hindering the global helium removal over a timescale compatible with AUG discharges. In both cases, the usual duration of an AUG discharge is not enough to remove all He particles. Only with both wall retention deactivated and enhanced pumping (simulation (4)) that the He content decays to 0 within the time of the discharge.

The results presented in this section show that if the employed cryopump is designed to efficiently remove helium, it may not be totally pumped within the time of a plasma discharge. The ‘delay’ in the permanent removal caused by several wall absorption/release cycles to which individual He atoms undergo before being pumped is closely linked to the intrinsic behavior of tungsten. Arbitrarily increasing the applied pumping speed may reduce this effect but never completely overrule it. Pollution of the plasma with some amount of helium is unavoidable for short-pulsed full-W tokamaks, if the wall has been somehow loaded with helium, because of the continuous release of this from the wall surfaces.

### 5.3. Implications for impurity transport and exhaust studies

The presented modeling results have highlighted that the walls play a major role in acting as dynamic sources and sinks for impurity particles in the plasma, at least for the case of helium in a short-pulsed full-W tokamak. The absolute number of He



**Table 2.** Global particle balance for the four simulations shown in figure 14. The columns contain (from left to right): initial and final total number of He particles within plasma + neutrals reservoirs; initial and final total number of He atoms implanted into the walls; total source (+) or sink (−) effect given by the walls and by the pump, respectively, for plasma + neutrals reservoirs; particles removed from plasma and neutrals reservoirs (also in percentage w.r.t. the initial value).

Simulation	Plasma + neutrals (initial)	Plasma + neutrals (final)	Walls (initial)	Walls (final)
(1)	$1.38 \times 10^{20}$	$0.42 \times 10^{20}$	$9.13 \times 10^{20}$	$8.90 \times 10^{20}$
(2)	$1.38 \times 10^{20}$	$0.10 \times 10^{20}$	—	—
(3)	$1.38 \times 10^{20}$	$0.15 \times 10^{20}$	$9.13 \times 10^{20}$	$4.47 \times 10^{20}$
(4)	$1.38 \times 10^{20}$	$0.00 \times 10^{20}$	—	—
Simulation	Wall source/sink	Pump sink	Net balance for plasma + neutrals reservoirs	
(1)	$+0.23 \times 10^{20}$	$-1.19 \times 10^{20}$	$-0.96 \times 10^{20}$ ( <b>70% removed</b> )	
(2)	—	$-1.28 \times 10^{20}$	$-1.28 \times 10^{20}$ ( <b>93% removed</b> )	
(3)	$+4.66 \times 10^{20}$	$-5.89 \times 10^{20}$	$-1.23 \times 10^{20}$ ( <b>89% removed</b> )	
(4)	—	$-1.38 \times 10^{20}$	$-1.38 \times 10^{20}$ ( <b>100% removed</b> )	

atoms dynamically retained within the walls in our main simulation is about one order of magnitude larger than the sum of He particles dynamically contained in the plasma and neutrals reservoirs. Temporary retention of He atoms in the walls contributes to slowing down the permanent removal of helium at AUG in a quantitatively similar way to what the lack of an efficient pumping system does. This suggests that any attempt to fit the time-dependent helium behavior with models that do not make use of wall reservoirs for long-term particle storage may result in a misleading physics interpretation of the observed exhaust.

From the modeling results, we also note that the simulated He density profiles at the edge are strongly affected by the plasma–wall interactions. Reflected and sputtered He atoms from the main wall are indeed energetic, and a deeper penetration up to the pedestal top is modeled. The additional particle source by ionization of the recycled neutrals has an impact on the modeled density profiles even with fixed transport (in terms of  $\nu/D$  ratio). This does not happen in the inner core, where the particle source by recycled neutrals is instead negligible, in agreement with the assumptions made in [28]. This implies that a correct assessment of main wall recycling does affect the experimental inference of impurity transport at the plasma edge (or, vice versa, the prediction of the pedestal profiles given prescribed transport coefficients). We suggest taking this into account in future edge transport studies for recycling impurities.

A further implication of our results is the impossibility to quantitatively estimate divertor retention of recycling impurities from experiments through analytical models, unless wall saturation is reached, relying solely on core plasma measurements. Roth *et al* inferred impurity compression by applying a multi-reservoir model similar to the one that we employed, fitting time-dependent impurity density measurements from the core plasma [77]. This is possible only as long as there are no other net particle sources or sinks for the plasma, apart from exchange with the divertor neutrals reservoir. The presence of a fully recycling wall is one basic assumption for the analytic equations describing such a model. The model of Roth *et al* was successfully used to estimate He compression,

relying only on core measurements, in previous studies at AUG with a full-C wall [13–15]. We assume that the poorer retention capability of helium in carbon may have resulted in a wall closer to saturation, fulfilling the basic assumptions of the model of Roth *et al*. We have shown that for the case of helium in a full-W machine, the wall is far from being saturated, and such a model may not be applied. A necessary ingredient for the application of our model to quantify the wall effects and interpret the exhaust dynamics in the full-W AUG is the possibility to consider He compression as an input, rather than require it as an output, thanks to the combination of measurements from CXRS and *in situ* Penning gauge. The modeling of the dynamic absorption and release rates from the walls is indeed constrained by the requirement of the modeled He compression being the same as the experimentally measured one. This is possible, thanks to a proper imposition in the model of a divertor retention time (see appendix B).

This highlights the extraordinary importance of having reliable partial pressure measurements of impurities in the exhaust gas. For ITER, it is planned to employ residual gas analyzers for such a task [78]. This solution does not find good applicability for short-pulsed devices, like AUG, because of the response time and time resolution of mass spectrometers, both being of the order of seconds, but it may be successful for ITER-relevant discharge timescales. Additionally, mass spectrometers cannot be placed within the vacuum vessel because of the detrimental influence of the magnetic field on them. Optical Penning gauges are, at the moment, the only solution that allows measuring impurity partial pressures in the exhaust gas directly at the divertor.

## 6. Summary and outlook

We experimentally investigated helium exhaust at the AUG tokamak by measuring the time-dependent He concentration both in the plasma and in the exhaust gas. We interpreted the observed exhaust dynamics with a novel multi-reservoir particle balance model, which accounts for plasma impurity transport, neutrals recycling and pumping, and wall retention.

The measured He compression increases with divertor neutral pressure. This indicates an improved divertor retention. On the other hand, He enrichment decreases. This indicates an increased dilution of helium in the exhaust gas. We also observed a slower helium removal when the divertor transits from an attached to a detached regime. These observations are qualitatively consistent with what has been observed at AUG with different divertor geometry and wall materials [13–15]. Albeit other elements might play a role in determining divertor retention of recycled He atoms, this strengthens the extrapolation of the observed behavior toward future fusion reactors.

In the interpretation of the experimentally observed exhaust dynamics, we saw that long-term storage of He atoms within the W wall plays a major role. This is explained by an efficient helium retention in tungsten [26] and the poor pumping capability of the AUG pumping systems for helium. The slow removal of helium from the system by active pumping increases the time in which it may recirculate throughout the machine, increasing in turn its probability to interact (and hence be absorbed) by the walls. Wall pumping is, however, not permanent since the retained atoms may be released later, constituting a new source for the plasma. The net effect is delaying the permanent removal of individual He particles from the system.

The model we employed made use of the experimental measurements of divertor retention of helium, which we observed to be independent of the exhaust dynamics, solely as an input. Other than the theoretical considerations presented in section 3, no quantitative attempts were made to clarify the behavior of divertor retention of helium as a function of the divertor plasma characteristics. This is left to a currently ongoing investigation, aimed at simulating the impact of several divertor plasma parameters on He compression with SOLPS-ITER.

The presented experimental studies were finalized for an assessment of helium exhaust in the most basic divertor plasma scenarios, i.e. type-I ELMy H-modes. We suggest extending this type of investigation also toward more advanced scenarios. Further efforts should be made to characterize helium pumping, e.g. in exhaust-oriented ELM-free H-mode scenarios, such as EDA (Enhanced D-Alpha) H-mode [79], quasi-continuous exhaust (QCE) regime [80], x-point radiating (XPR) regime [81], compact radiative divertor (CRD) [82], or in ELM-suppressed H-modes through resonant magnetic perturbations (RMPs) [83, 84]. Investigations into alternative divertor configurations, such as X-divertor and snowflake divertor, may also be performed in the near future at AUG, after the completed installation of a new upper divertor with in-vessel coils [85]. This will be possible, thanks to the presence of a cryopump coated with activated charcoal to trigger He cryosorption [86].

## Acknowledgments

This work has been carried out within the framework of the EUROfusion Consortium, funded by the European Union via the Euratom Research and Training Programme (Grant

Agreement No. 101052200—EUROfusion). The views and opinions expressed are, however, those of the author(s) only and do not necessarily reflect those of the European Union or the European Commission. Neither the European Union nor the European Commission can be held responsible for them.

## Appendix A. Definition of dynamic wall loads for wall retention modeling

For a correct modeling of helium release from the wall due to ion bombardment, the total ion fluxes of the background plasma species striking the walls in the experiment have to be assumed in the helium simulations (equation (13)). For the presented case, D and N fluxes are required. These were achieved running Aurora simulations for the background plasma, i.e. for deuterium and nitrogen separately, consistently with the available measurements from the experiment. These fluxes, found as output from the deuterium/nitrogen simulations, are then used as input for the helium simulation. Such background simulations feature a constant numerical solution (apart from ELM events), relying on the assumption of deuterium and nitrogen being constant in the experiment while the evolution of helium is considered. The top plots in figure 15 show the values of inter- and intra-ELM D and N fluxes onto the main and divertor walls, achieved in this way and used to define the background wall loads for the presented helium simulation for discharge #39149. Such time-dependent pattern is repeated for the entire duration of the helium simulations. The assumed values of about  $0.5 \times 10^{23}$  ions  $s^{-1}$  for the inter-ELM phases and about  $2.5 \times 10^{23}$  for the ELM peak for the divertor wall load are consistent with the measurements of the Langmuir probes. The top right plot in figure 15 shows how the imposed D particle flux compares well with the Langmuir probe measurements: the red points represent the original measurements of the total ion flux (achieved integrating the measured ion flux density profiles onto both the inner and outer target surfaces) synchronized over multiple ELM events in discharge #39149, while the black line is the conditional average of such data [87]. The estimates of the N fluxes are based on the assumption of the N partial pressure correlating with the external N gas puff rather than with the core N concentration [88]. In other words, as in the discharge #39149 N fueling is 3% of the D fueling (if expressed in ions  $s^{-1}$ ), then the N partial pressure is also 3% of the D partial pressure. Therefore, as the partial pressure is strongly coupled to the recycling fluxes from the wall, the assumed N fluxes onto the walls in figure 15 are also 3% of the assumed D fluxes.

An assumption about the mean ion impact energy onto the main and divertor walls is also needed, not only for deuterium and nitrogen but also for helium itself, in order to consider realistic values for both reflection coefficients (used in equations (9) and (10)) and sputtering yields (used in equation (13)). The bottom plots in figure 15 show the values of inter- and intra-ELM impact energy for helium, deuterium, and nitrogen onto the main and divertor walls assumed for the presented simulations of discharge #39149. Again, such



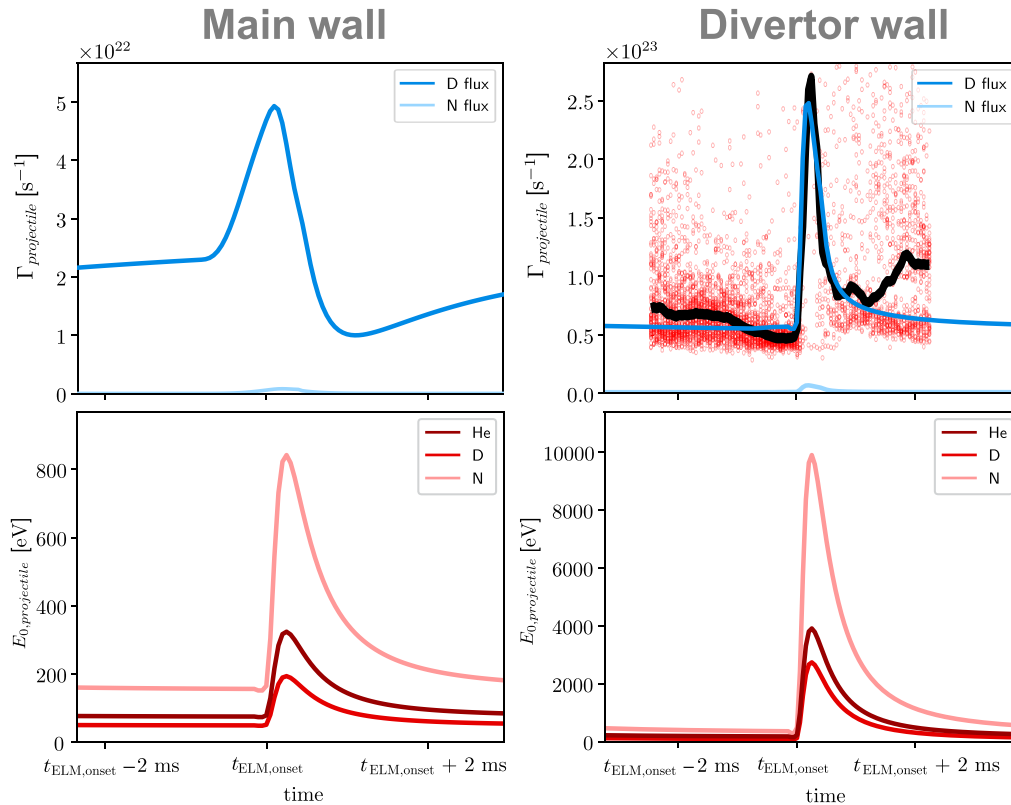


**Figure 15.** Time traces of the background ion fluxes (top plots) and He + background impact energies (bottom plots), used as input for the presented He simulations, during each ELM cycle. The experimentally measured total particle flux onto the divertor targets for discharge #39149 is also shown for comparison (original data as red points; conditional average as a black solid line). The shown patterns are repeated for the entire duration of the performed He simulations with a constant frequency set as the experimentally measured average ELM frequency (which is 125 Hz for discharge #39149). For the calculation of the impact energies at the main wall, we considered  $T_{e,\text{main}} = 10$  eV in inter-ELM phases and  $T_{e,\text{main}} = 30$  eV at the ELM peak. For the divertor wall, instead, we considered  $T_{e,\text{div}} = 15$  eV in inter-ELM phases and  $T_{e,\text{ped}} = 600$  eV for the application of the free streaming model at the ELM peak. These values are also consistent with the measurements from discharge #39149.

time-dependent pattern is repeated for the entire duration of the helium simulations. Generally, the ion impact energy onto a material surface is estimated as given by the sum of the kinetic energy of the ions plus a contribution caused by sheath acceleration, i.e. as  $E_0 = 2T_i + 3ZT_e$  [89]. Therefore, one only needs to know the plasma temperature at the plasma–material interfaces and the mean charge state of the ion projectile. The latter can be estimated, also knowing the plasma temperature assuming coronal equilibrium. This is how the impact energies for the various projectiles, shown in figure 15, are chosen.

An exception is the peak energy value during ELMs at the divertor. For estimating this, we employ the so-called free-streaming model [90, 91]. This relies on the assumption of the parallel energy flux from the pedestal not limited by the sheath within ELM filaments. Therefore, the peak impact energy during ELM is assumed to be simply proportional to the pedestal plasma temperature, i.e.  $E_{0,\text{div,ELM}} = \alpha T_{e,\text{ped}}$ . The peak values in the bottom right plot in figure 15 are found in this way, employing the measured pedestal temperature from the experiment. The proportionality coefficients for each species were calculated analytically according to [91]. The values up to several thousands of electron volts, which may be assumed at the ELM peaks, are supported by experimental observations [73].

However, looking at the surface coefficients in figure 11, we note that at energy roughly above 500 eV, the energy dependence of the surface coefficients becomes much less relevant. Therefore, a precise estimate of the ion impact energies at the ELM peak does not have a great impact to our modeling. To this regard, according to a recent publication, the free-streaming estimate of the intra-ELM ion impact energies, which we employ, may be overestimated by up to a factor of 3 [92]. Even considering this, the impact energies at the ELM peak would be still at the order of one to few thousands of electron volts, i.e. at the high energy branch of the surface coefficient curves. Therefore, we believe that this possible overestimation of the ELM impact energies does not qualitatively affect the outcome of our modeling.

## Appendix B. Sensitivity analyses on free input parameters for dynamic He exhaust modeling

Our newly developed model features a large number of input parameters. Many of these are to be considered free parameters. To set appropriate values for such free parameters, sensitivity analyses were performed. Simulations were run, varying

one input parameter individually, with all other input parameters kept fixed. The results were contrasted against the available experimental data, i.e. He ion density in the plasma and He neutral atom content in the exhaust gas. The most appropriate values for all the free parameters were then taken as the ones ensuring the best fit with the experimental data. The results of the sensitivity analysis on few of such parameters, applied to AUG discharge #39149, are presented here.

- Divertor retention time  $\tau_{\text{ret}}$  is the parameter describing the backflow of He particles from the divertor reservoir toward the plasma (equation (6)). Assuming fixed core transport (hence a fixed core confinement time  $\tau_{\text{main}}$ ), such time is directly coupled with the He compression, as it can be shown that

$$C_{\text{He}} \approx \frac{V_{\text{plasma}}}{V_{\text{div}}} \frac{\tau_{\text{ret}}}{\tau_{\text{main}}}. \quad (\text{B1})$$

Therefore, different imposed divertor retention times produce different ratios between He content in the plasma and in the divertor (top left plots in figure 16). The most appropriate value is the one ensuring then a value of such a ratio being the experimentally observed one. For the presented case, the most appropriate value of this parameter was 4 ms.

- Pumping speed  $S_{\text{pump}}$  is the parameter describing the permanently removed flux from the pump reservoir (equation (8)). This is not an actual free parameter, as what we used was the experimentally measured value of  $7 \text{ m}^3 \text{ s}^{-1}$  from the AUG turbomolecular pumping system [30]. This measurement holds for deuterium, but since He atoms and D molecules have nearly the same mass, we can assume the effect of a purely mechanical pumping system to be similar. The performed sensitivity analysis (bottom left plots in figure 16) shows that increasing the applied pumping speed of a factor of 2–3 produces a speedup of the helium removal, which is, however, not dramatic. Only by enhancing the pumping speed of a more than an order of magnitude, as shown in figure 14, would enhance the exhaust in a relevant way.
- Saturation densities  $\sigma_{\text{imp,wall}}^{\text{sat}}$  of helium implanted into the main and divertor walls are the parameters that limit the number of He atoms that can be dynamically stored in the wall reservoirs (equation (4)). The performed sensitivity analysis (top right plots in figure 16) shows that, increasing such parameters, the wall pumping effect becomes more relevant when an external He injection is applied. In this case, applying the same He gas puff results in a minor increase in the He content in the plasma and in the neutral gas. The reason is a larger fraction of the injected He particles being promptly absorbed by the walls. For the presented case, the most appropriate values of such parameters were  $3 \times 10^{19}$  He atoms per  $\text{m}^2$  for the main wall and  $6 \times 10^{19}$  He atoms per  $\text{m}^2$  for the divertor wall. These values are in good agreement with the retention measurements of helium implanted in tungsten [26]. A larger value for the divertor wall is to be expected because of the higher average impact energies.

- Roughness factor multiplies the geometric main and divertor wall surface areas (which are 5 and  $0.5 \text{ m}^2$ , respectively) when converting He implantation densities into absolute number of implanted atoms in the wall retention calculations. The performed sensitivity analysis (bottom right plots in figure 16) shows that the effect of increasing such a parameter is similar to the effect of increasing the wall saturation densities. In both cases, the maximum absolute numbers of He atoms that the walls can dynamically accommodate increase. We note that multiplying the geometric areas of a factor of 60 is required to correctly reproduce the experimentally observed dynamics. If this was smaller, the walls would not be able to accommodate a sufficient absolute number of He atoms to reproduce the experimental measurements in the plasma and in the exhaust gas. The need for effective surface areas larger than the geometric plasma-wetted areas for wall retention calculations is not surprising; plasma-exposed W PFCs indeed show a roughness, which is orders of magnitude larger than the depth of He implantation profiles in tungsten [76].

### Appendix C. Initial conditions for wall inventories for dynamic He exhaust modeling

As for any dynamic model, a successful application of our newly developed model described in section 4 requires an appropriate choice of initial conditions for all the dynamic particle reservoirs. In the case of AUG discharge #39149, these are referred to  $t = 2.2 \text{ s}$  (figure 12). The application of initial conditions for plasma and neutrals reservoirs (in terms of volume densities) is trivial, as the required values are the ones given by the experiment. Instead, the initial conditions for the wall reservoirs (in terms of surface densities) are unknown and should be considered as further free parameters for the model.

We found that such initial conditions may be self-consistently chosen, studying the behavior of the model itself. Figure 17 shows the impact on the simulation results of imposing different initial conditions for the main and divertor wall reservoirs separately, with all other input parameters being unchanged.

For the main wall, imposing different initial conditions implies modeling a faster or slower decay of the He content in the plasma after the active injection phase, with the relevant recycling/pumping parameters (e.g. divertor retention time and pumping speed) being unchanged. This is consistent with the main wall being identified as a net absorber of He atoms throughout plasma discharges; how much helium is already implanted into it at the beginning of a discharge will indicate how many more He atoms it can accommodate before reaching equilibrium and how quickly it absorbs them.

For the divertor wall, imposing different initial conditions implies different responses of the model to the initial conditions for plasma and neutrals reservoirs. If the initial divertor wall content is ‘too high’, then the modeled time traces for plasma/neutrals jump toward larger values than the experimental ones. Indeed, if the modeled He content in the wall

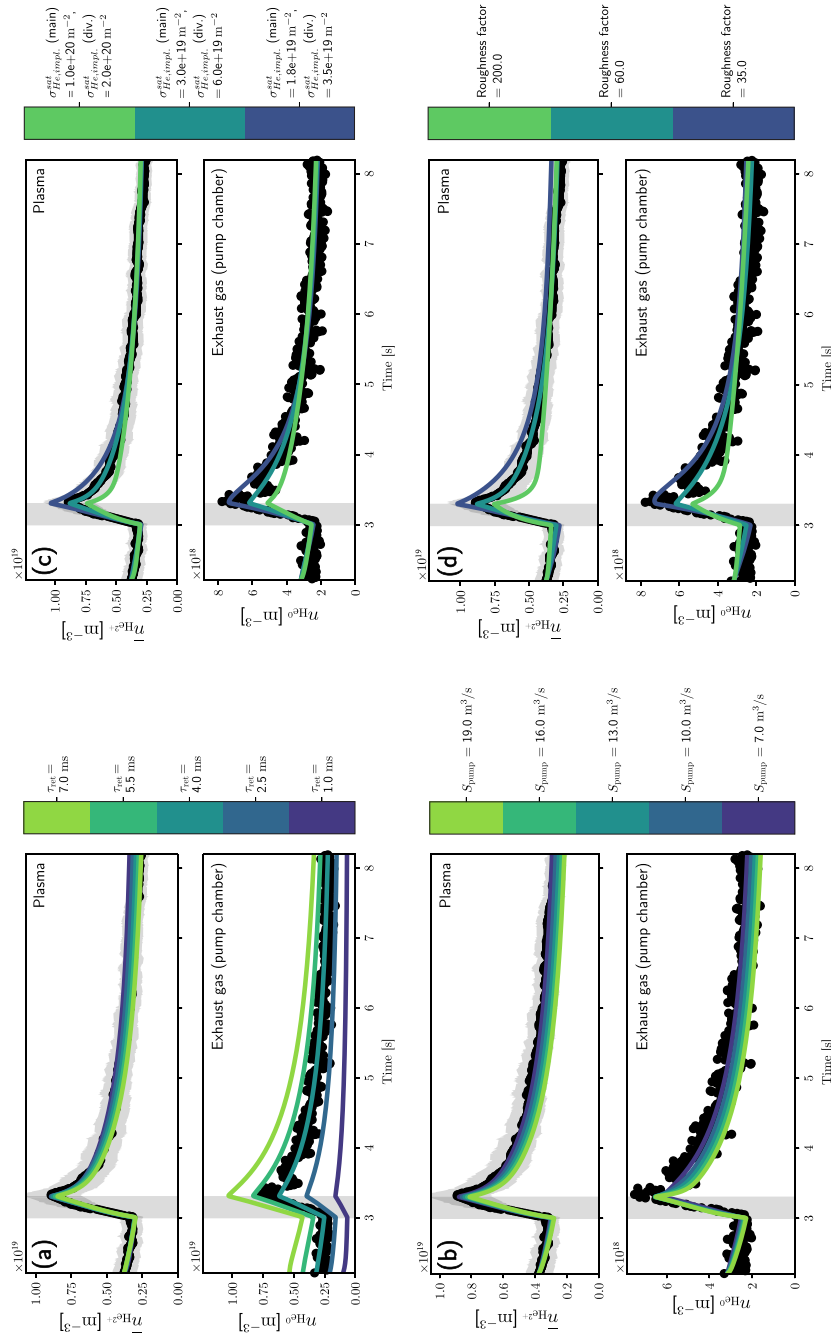


**Figure 16.** Results of performing sensitivity analyses on several input parameters, based on the modeling of AUG discharge #39149. Only the plasma reservoir and pump reservoir are shown. The individually varied input parameters are (a) divertor retention time, (b) pumping speed, (c) wall saturation values, and (d) wall roughness factor.

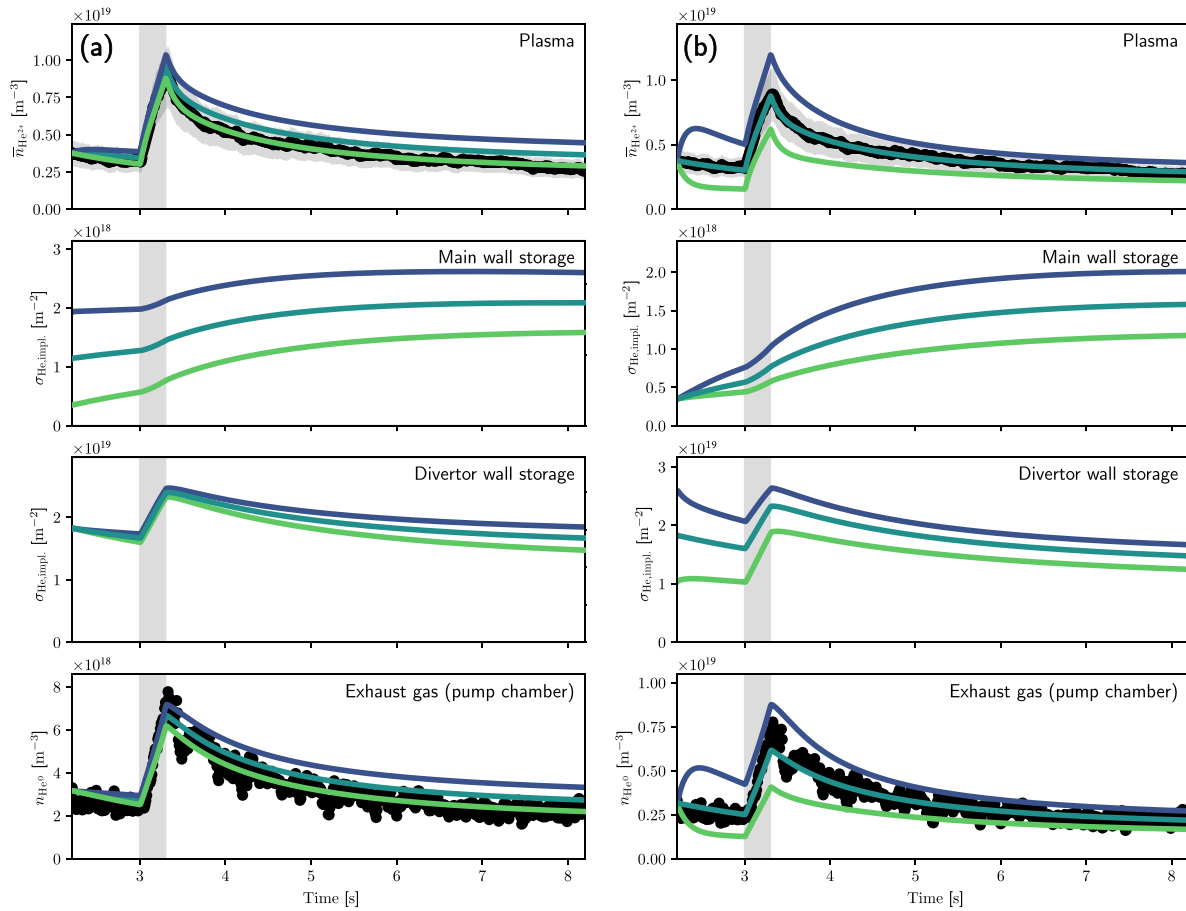


**Figure 17.** Sensitivity analysis of the modeling results over different initial conditions. (a) Different colors indicate simulations performed with three different initial conditions for the main wall reservoir (see second plot from top). (b) Different colors indicate simulations performed with three different initial conditions for the divertor wall reservoir (see third plot from top). All other input parameters are kept the same.

is higher than in the reality, then also the modeled dynamic He particle release is too large to be compatible with the experimental plasma/neutrals initial conditions. This occurs although the relevant plasma–wall interaction parameters (e.g. background fluxes toward walls and surface coefficients) are unchanged. Conversely, if the initial divertor wall content is ‘too low’, then the dynamic He particle release is too low as well, and the modeled time traces for plasma/neutrals drop toward smaller values than the experimental ones.

From this, we conclude that there is one and only one initial condition for these reservoirs, which is compatible with the experimentally known initial conditions for plasma/neutrals. Therefore, such initial conditions for the wall reservoirs may be fitted to reproduce the experimental observations as for the free parameters present in the model equations. Their values may be selected through the application of the model in a self-consistent way, with a trial-and-error procedure, to find values that ensure the desired modeled behavior of the plasma and neutrals reservoirs.

The fact that a higher content of initially implanted helium in the walls translates into a higher simulated He content in the plasma/gas, even with otherwise identical input parameters,

is also consistent with the experimentally observed impact of boronizations on AUG plasmas [93, 94], during which helium is implanted while performing He glow discharges. The measured amount of helium in discharges (with no active He seeding), otherwise identical but at different time distances from boronizations (e.g. standard H-modes), is indeed different, with He content being higher in discharges soon after a boronization w.r.t. later.

## ORCID iDs

- A. Zito <https://orcid.org/0000-0002-6743-6568>  
A. Kappatou <https://orcid.org/0000-0003-3341-1909>  
A. Kallenbach <https://orcid.org/0000-0003-0538-2493>  
F. Sciortino <https://orcid.org/0000-0002-5159-1889>  
E.T. Hinson <https://orcid.org/0000-0001-9713-140X>  
O. Schmitz <https://orcid.org/0000-0002-9580-9149>  
M. Cavedon <https://orcid.org/0000-0002-0013-9753>  
R.M. McDermott <https://orcid.org/0000-0002-8958-8714>  
M. Griener <https://orcid.org/0000-0003-2953-536X>  
U. Stroth <https://orcid.org/0000-0003-1104-2233>

## References

- [1] Reiter D., Wolf G.H. and Kevers H. 1990 *Nucl. Fusion* **30** 2141
- [2] Reiter D., Wolf G.H. and Kevers H. 1990 *J. Nucl. Mater.* **176–177** 756–62
- [3] Reiter D., Kevers H., Wolf G.H., Baelmans M., Behrisch R. and Schneider R. 1991 *Plasma Phys. Control. Fusion* **33** 1579
- [4] Pütterich T., Fable E., Dux R., O'Mullane M., Neu R. and Siccino M. 2019 *Nucl. Fusion* **59** 056013
- [5] Loarte A. et al (The ITPA Scrape-off Layer and Divertor Physics Topical Group) 2007 Chapter 4: power and particle control *Nucl. Fusion* **47** S203
- [6] McDonald D.C. et al 2004 *Plasma Phys. Control. Fusion* **46** 519–34
- [7] Ryter F. et al 2009 *Nucl. Fusion* **49** 062003
- [8] Kappatou A. et al 2018 Energy confinement and performance of pure helium plasmas and helium seeded deuterium plasmas 2018 IAEA Fusion Energy Conf. (Gandhinagar, 22–27 October 2018) (available at: <https://nucleus.iaea.org/sites/fusionportal/Shared%20Documents/FEC%202018/fec2018-preprints/preprint0485.pdf>)
- [9] Abdou M., Riva M., Ying A., Day C., Loarte A., Baylor L.R., Humrickhouse P., Fuerst T.F. and Cho S. 2021 *Nucl. Fusion* **61** 013001
- [10] Groth M. et al 2001 *J. Nucl. Mater.* **290–293** 867–71
- [11] Groth M. et al 2002 *Nucl. Fusion* **42** 591–600
- [12] Zastrow K.-D. et al 2005 *Nucl. Fusion* **45** 163–75
- [13] Bosch H.-S. et al 1997 *Plasma Phys. Control. Fusion* **39** 1771–92
- [14] Bosch H.-S., Ullrich W., Bard A., Coster D., Haas G., Kallenbach A., Neuhauser J. and Schneider R. (ASDEX Upgrade Team) 1999 *J. Nucl. Mater.* **266–269** 462–6
- [15] Bosch H.-S., Ullrich W., Coster D., Gruber O., Haas G., Neuhauser J., Schneider R. and Wolf R. 2001 *J. Nucl. Mater.* **290–293** 836–9
- [16] Sakasai A., Takenaga H., Kubo H., Akino N., Higashijima S., Sakurai S., Tamai H., Itami K. and Asakura N. 2001 *J. Nucl. Mater.* **290–293** 957–61
- [17] Wade M.R. et al 1995 *J. Nucl. Mater.* **220–222** 178–82
- [18] Wade M.R. et al 1998 *Nucl. Fusion* **38** 1839
- [19] Coster D.P., Bosch H.-S. and Ullrich W. 2001 *J. Nucl. Mater.* **290–293** 845–8
- [20] Reiser D., Schneider R., Coster D., Ullrich W. and Bosch H.S. 2001 *J. Nucl. Mater.* **290–293** 953–6
- [21] Kukushkin A.S., Pacher H.D., Kotov V., Reiter D., Coster D. and Pacher G.W. 2007 *Nucl. Fusion* **47** 698–705
- [22] Pacher G.W., Pacher H.D., Janeschitz G. and Kukushkin A.S. 2008 *Nucl. Fusion* **48** 105003
- [23] Pacher H.D., Kukushkin A.S., Pacher G.W., Kotov V. and Reiter D. 2011 *J. Nucl. Mater.* **415** S492–6
- [24] Pacher H.D., Kukushkin A.S., Pacher G.W., Kotov V., Pitts R.A. and Reiter D. 2015 *J. Nucl. Mater.* **463** 591–5
- [25] Neu R. et al 2005 *Nucl. Fusion* **45** 209–18
- [26] Schmid K., Schwarz-Selinger T., Jacob W. and Dux R. 2007 *Nucl. Fusion* **47** 984–9
- [27] Herrmann A. and Gruber O. 2003 *Fusion Sci. Technol.* **44** 569–77
- [28] Kappatou A. et al 2019 *Nucl. Fusion* **59** 056014
- [29] Streibl B., Kaltenberger A., Kollotzek H., Mattes K., Rohde V., Schall G. and Schindler K. 2001 *Fusion Eng. Des.* **56–57** 867–72
- [30] Rohde V., Mertens V. and Scarabosio A. 2009 *J. Nucl. Mater.* **390–391** 474–7
- [31] Kim J., Schaubel K.M. and Colleraine A.P. 1990 *J. Vac. Sci. Technol. A* **8** 3084
- [32] Isler R.C. et al 1994 *Plasma Phys. Control. Fusion* **36** 171
- [33] McDermott R.M. et al 2018 *Plasma Phys. Control. Fusion* **60** 095007
- [34] Summers H.P., Dickson W.J., O'Mullane M.G., Badnell N.R., Whiteford A.D., Brooks D.H., Lang J., Loch S.D. and Griffin D.C. 2006 *Plasma Phys. Control. Fusion* **48** 263–93
- [35] Fonck R.J., Darrow D.S. and Jaehnig K.P. 1984 *Phys. Rev. A* **29** 3288
- [36] Kappatou A., McDermott R.M., Pütterich T., Dux R., Geiger B., Jaspers R.J.E., Donné A.J.H., Viezzer E. and Cavedon M. 2018 *Plasma Phys. Control. Fusion* **60** 055006
- [37] Kremeyer T., Flesch K., Schmitz O., Schlisio G. and Wenzel U. 2020 *Rev. Sci. Instrum.* **91** 043504
- [38] Penning F.M. 1936 *Physica* **3** 873
- [39] Hillis D.L., Klepper C.C., Von Hellermann M., Ehrenberg J., Finken K.H. and Mank G. 1997 *Fusion Eng. Des.* **34–35** 347
- [40] Bosch H.-S. et al 1996 *Phys. Rev. Lett.* **76** 2499–502
- [41] Kallenbach A. et al 2021 *Nucl. Fusion* **61** 016002
- [42] Haas G. and Bosch H.-S. 1998 *Vacuum* **51** 39–46
- [43] Schneider R. et al 1999 *J. Nucl. Mater.* **266–269** 175–81
- [44] Kallenbach A. et al 2010 *Plasma Phys. Control. Fusion* **52** 055002
- [45] Schneider P.A. et al 2014 *Plasma Phys. Control. Fusion* **56** 025011
- [46] Pütterich T., Dux R., Janzer M.A. and McDermott R.M. 2011 *J. Nucl. Mater.* **415** S334–9
- [47] Stangeby P.C. and Elder J.D. 1995 *Nucl. Fusion* **35** 1391
- [48] Shimizu K. et al 1997 *J. Nucl. Mater.* **241–243** 167–81
- [49] Stangeby P.C. and Moulton D. 2020 *Nucl. Fusion* **60** 106005
- [50] Senichenkov I.Y., Kaveeva E.G., Sytova E.A., Rozhansky V.A., Voskoboinikov S.P., Veselova I.Y., Coster D.P., Bonnin X. and Reimold F. 2019 *Plasma Phys. Control. Fusion* **61** 045013
- [51] Hitzler F., Wischmeier M., Reimold F. and Coster D.P. 2020 *Plasma Phys. Control. Fusion* **62** 085013
- [52] Rohde V., Kallenbach A., Mertens V. and Neu R. 2009 *Plasma Phys. Control. Fusion* **51** 124033
- [53] Dux R. 2006 *IPP Report* 10-30 (Max-Planck-Institut für Plasmaphysik)
- [54] Stangeby P.C. and Elder J.D. 1992 *J. Nucl. Mater.* **196–198** 258–63
- [55] Schmid K., Reinelt M. and Krieger K. 2011 *J. Nucl. Mater.* **415** S284–8
- [56] Schmid K., Krieger K., Lisgo S.W., Meisl G. and Brezinsek S. 2015 *J. Nucl. Mater.* **463** 66–72
- [57] Meisl G., Schmid K., Encke O., Höschen T., Gao L. and Linsmeier C. 2014 *New J. Phys.* **16** 093018
- [58] Meisl G., Schmid K., Krieger K., Oberkofler M. and Lisgo S.W. (JET Contributors) 2016 *Phys. Scr.* **T167** 014079
- [59] Sciortino F. et al 2021 *Plasma Phys. Control. Fusion* **63** 112001
- [60] Dux R., Janzer A. and Pütterich T. 2011 *Nucl. Fusion* **51** 053002
- [61] Dux R. 2003 *Fusion Sci. Technol.* **44** 708–15
- [62] Fajardo D., Angioni C., Maget P. and Manas P. 2022 *Plasma Phys. Control. Fusion* **64** 055017
- [63] Cavedon M. et al 2017 *Plasma Phys. Control. Fusion* **59** 105007
- [64] Fischer R., Fuchs C.J., Kurzan B., Suttrop W. and Wolfrum E. 2010 *Fusion Sci. Technol.* **58** 675–84
- [65] Willensdorfer M., Birkenmeier G., Fischer R., Lagner F.M., Wolfrum E., Veres G., Aumayr F., Carralero D., Guimarães L. and Kurzan B. 2014 *Plasma Phys. Control. Fusion* **56** 025008



- [66] Kurzan B. and Murmann H.D. 2011 *Rev. Sci. Instrum.* **82** 103501
- [67] Rathgeber S.K., Barrera L., Eich T., Fischer R., Nold B., Suttrop W., Willensdorfer M. and Wolfrum E. 2013 *Plasma Phys. Control. Fusion* **55** 025004
- [68] Viezzer E., Pütterich T., Dux R. and McDermott R.M. 2012 *Rev. Sci. Instrum.* **83** 103501
- [69] Biersack J.P. and Eckstein W. 1984 *Appl. Phys. A* **34** 73–94
- [70] Eckstein W. 1994 *Radiat. Eff. Defects Solids* **130–131** 239–50
- [71] Eckstein W. 2002 *IPP Report* 9-132 (Max-Planck-Institut für Plasmaphysik)
- [72] Schmid K., Mayer M., Adelhelm C., Balden M. and Lindig S. 2010 *Nucl. Fusion* **50** 105004
- [73] Guillemaut C. et al 2015 *Plasma Phys. Control. Fusion* **57** 085006
- [74] Küstner M., Eckstein W., Dose V. and Roth J. 1998 *Nucl. Instrum. Methods Phys. Res. B* **145** 320–31
- [75] Cupak C. et al 2021 *Appl. Surf. Sci.* **570** 151204
- [76] Hakola A. et al 2014 *Phys. Scr.* **T159** 014027
- [77] Roth J., Krieger K. and Fussmann G. 1992 *Nucl. Fusion* **32** 1835
- [78] Klepper C.C. et al 2015 *Fusion Eng. Des.* **96–97** 803–7
- [79] Gil L. et al 2020 *Nucl. Fusion* **60** 054003
- [80] Harrer G.F. et al 2022 *Phys. Rev. Lett.* **129** 165001
- [81] Bernert M. et al 2021 *Nucl. Fusion* **61** 024001
- [82] Lunt T., Bernert M., Brida D., David P., Faitsch M., Pan O., Stieglitz D., Stroth U. and Redl A. 2023 *Phys. Rev. Lett.* **130** 145102
- [83] Suttrop W. et al 2018 *Nucl. Fusion* **58** 096031
- [84] Hinson E.T. et al 2020 *Nucl. Fusion* **60** 054004
- [85] Lunt T., Zohm H., Herrmann A., Kallenbach A., Dunne M., Feng Y., Neu R. and Wischmeier M. 2017 *Nucl. Mater. Energy* **12** 1037–42
- [86] Schall G., Berger N., Bösler D., Herrmann A., Rohde V., Sochor M. and Weißgerber M. 2021 *Fusion Eng. Des.* **166** 112316
- [87] Laggner F.M. et al 2018 *Plasma Phys. Control. Fusion* **60** 025002
- [88] Drenik A. et al 2019 *Nucl. Fusion* **59** 046010
- [89] Kallenbach A. et al 2011 *J. Nucl. Mater.* **415** S19–S26
- [90] Fundamenski W. and Pitts R.A. (JET EFDA Contributors) 2006 *Plasma Phys. Control. Fusion* **48** 109–56
- [91] Moulton D., Ghendrih P., Fundamenski W., Manfredi G. and Tskhakaya D. 2013 *Plasma Phys. Control. Fusion* **55** 085003
- [92] Horacek J. et al 2023 *Nucl. Fusion* **63** 056007
- [93] Rohde V., Dux R., Kallenbach A., Krieger K. and Neu R. 2007 *J. Nucl. Mater.* **363–365** 1369–74
- [94] Kallenbach A. et al 2009 *Nucl. Fusion* **49** 045007